MODELING THE THERMAL AND ELECTRICAL PROPERTIES OF DIFFERENT DENSITY SINTERED BINDER JETTED COPPER FOR VERIFICATION AND REVISION OF THE WIEDEMANN-FRANZ LAW

Matthew Paul Meeder

Thesis submitted to the Faculty of the
Virginia Polytechnic Institute and State University
in partial fulfillment of the requirements for the degree of

Masters
in
Science in Mechanical Engineering

Al L. Wicks, Chair
Scott T. Huxtable
Thomas E. Diller
Christopher B. Williams

June 7, 2016
Blacksburg, Virginia

Keywords: Additive Manufacturing, Copper, Binder Jet Printing, Wiedemann Franz Law, thermal conductivity , electrical conductivity

MODELING THE THERMAL AND ELECTRICAL PROPERTIES OF DIFFERENT DENSITY SINTERED BINDER JETTED COPPER FOR VERIFICATION AND REVISION OF THE WIEDEMANN-FRANZ LAW

Matthew Paul Meeder

(ABSTRACT)

There is a link between the thermal and electrical properties of metal. The equation which links these two properties is called the Wiedemann-Franz Law. Also there is an emerging technology within Additive Manufacturing called Binder Jet Printing which can print high purity copper without heat stress within the material. Due to the Binder Jet Printings ability to print high resolution prints without any print through, this makes future use of this technology a necessity for future electrical and thermal components within computers. However a thermal and electrical conductivity analysis of binder jetted copper has never been performed, and needs to be for simulation with this material. Therefore within this thesis the relationship of the thermal and electrical properties of printed binder jetted copper part will be researched.

To find the electrical resistivity of binder jetted copper, three sets of 2mm diameter rods where printed and then placed within a modified four wire resistance method test. For the thermal conductivity measurements a laser flash diffusivity machine was used, and three sets of 11 copper disks of approximately 1cm diameter by 1mm where printed.

The data shows a strong linear trend linking electrical resistivity to the density ratio of the copper. Within the thermal conductance measurement, more variability was seen within the three different prints. The 70 percent density ratio prints saw a large 13 percent spread in density ratios throughout the prints, which is believed to be caused by improper sintering due to temperature gradients near the door of the kiln. The 82 percent density prints saw better grouping of density ratios by placing the specimens in the back of the kiln. Lastly, the 92 percent prints saw the best density ratio grouping but the largest thermal conductivity variance. Even though the scatter plot for the thermal conductivity measurements are not as precise as the electrical resistivity measurements, it still shows a linear trend which matches the NASA data from 1971. Overall, these linear trends can be modeled and compiled into a new form of the Wiedemann-Franz law, which accounts for the density ratio of the binder jetted print.

Acknowledgments

My foremost thanks goes to God, who by His grace sustained through my bachelors and masters degree here at Virginia Tech. I would like to thank Dr. Wicks for advising be through my time here at Virginia Tech, and I would like to thank him for keeping me on the straight and narrow. I would like to also thank Dr. Williams for all his help in understanding Additive Manufacturing, and letting me use his Binder Jet machine. I would like to thank Yun Bai for all his help printing and sintering the test specimens. I would like to thank Dr. Huxtable for letting me use his laser flash rig for all the thermodynamic experiments. I would like to thank Jue Wang for helping me obtain the thermodynamic data, and run the laser flash rig. I would like to thank Dr. Diller for all his help throughout my undergraduate career helping me learn thermodynamics. I would last like to thank Dr. Sweeney for his time helping me set up and run the four wire resistance testing on the copper rods.

Contents

List of Figures

List of Tables

Chapter 1

History of Additive Manufacturing.

The beginning of additive manufacturing does not start with the first photolithography machines from 1987, but a century earlier with topographic mapping from the 1800s. [1] Finally patented in 1940s, this style of making 3D maps by layering paper and cardboard brought about the idea of using a series of "layers" to build up a 3D model. This style of topographical mapping therefore thought as a precursor to the concepts used for every additive manufacturing technology currently used today. Seen in Figure 1.1 is a topographical map of the Grand Canyon. Notice how through a series of layers of cardboard a three dimensional map can be created.

Figure 1.1: Topographical map of the Grand Canyon.

Also another technology which is accredited to helping progress of additive manufacturing is photosculpting [1]. Developed in the 1860's by Francois Willeme, this technology utilized 24

cameras to transfer the image onto 24 different silhouettes. Post processing these silhouettes around a sculpting medium will make a copy of the object photographed.

Using light to create a series of layers or "silhouettes" of an object is given credit for inspiring the first series of vat photopolymerization machines called stereolithography.

Seen in Figure 1.2 is The patent of Francois Willeme. It shows in its Figure 1 the apparatus of taking a series of pictures around an object for cerate a series of silhouettes. Figure 2 shows how the photographed object was translated and scaled correctly using a device shown in Figure 3 [1].

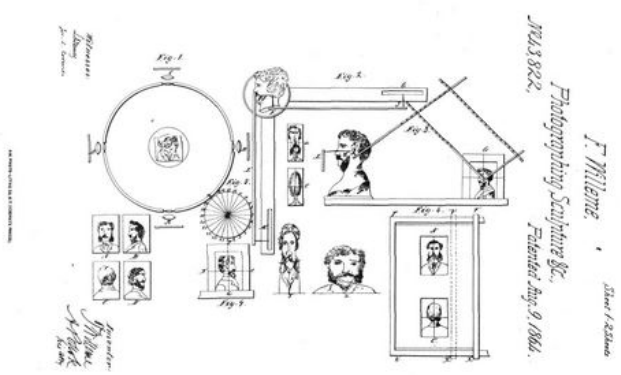

Figure 1.2: The patent submitted by Francois Willeme of his photosculpting technology

The first true additive manufacturing machine was a steriolithography (SL) machine developed by 3D systems in 1987. The process used UV sensitive liquid polymers and was solidified using a laser. Several other companies began developing SL machines, and then in 1991 three other style additive manufacturing technologies were commercialized. They were fused deposition modeling (FDM) by Stratysis, Solid ground curling (SGC) by Cubital, and Laminated object manufacturing (LOM) by Helisys. The first selective laser sintering (SLS) machines came to commercial market in 1992 by DTM. Throughout the past three decades, and even still today, more complex additive manufacturing machines are being designed and brought to commercial and private markets. Seen in the figure below are all the current and past methods used in additive manufacturing [2].

All of the technologies seen in the figure below and in additive manufacturing is based off of making a voxel. Think of a voxel as a three dimensional pixel. Simply enough, just as a picture on a television screen is made of a series of pixels, a voxel just adds the z dimension

to that picture. Also another good way to imagine a voxel is a 1 x 1 x 1 Lego brick sculpture, seen in the figure below are two different picture of the video game character Mario. To the left is an 8 bit recreation with 1x1 Lego blocks where each 1x1 block is representative of a pixel. To the right is a 3 dimensional recreation of the same image, where each of the 1x1x1 Lego blocks is representative of a voxel [3].

Figure 1.3: This is a series of two photos showing the difference between pixels and Voxels.

1.1 Types of Additive Manufacturing

Material Jetting is an additive manufacturing technology which is very similar to the inkjet printer in your house. Instead of printing different color inks, the material jetting printer prints different materials. The printer can print a rigid ABS plastic to the extreme of a soft rubber, therefore my varying the percentage of rubber voxels in the overall print, the flexibility can change per section of the print. Curing is performed by a UV light built into the injector shuttle and also post print in a UV oven. Currently in the biomedical field this is the style of additive manufacturing being used to create tissue, and other biological structures [4].

Material extrusion, also called fused deposition modeling is the most common method of additive manufacturing on the market today. This style of additive manufacturing creates its voxels by extruding a polymer in a single strand, and after finishing a layer, moves up one layer height and starts creating the next layer. Most simple way to envision this style of machine is a linear actuated hot glue gun, where the material is melted in the nozzle of

the extruder, extruded onto the build tray, and computer guided in the X, Y, and Z axis to accurately create the STL file [4].

Powder bed fusion is a method of creating additive manufacturing parts by melting a preheated powder bed with a laser. The voxel is created by melting a small portion of heated powder by a laser, and by moving the laser across the powder bed in a controlled fashion, can quickly create on layer of the STL file. This is one way metal can be currently printed and will be discussed later [4].

Vat photopolymerization is the oldest style of additive manufacturing and uses a laser to cure a photo sensitive liquid polymer in order to create the voxel. By re-layering with dunking into the photo sensitive liquid, and hardening layer after layer with the laser, the total shape of the desired part can be created [4].

Last but not least is sheet lamination, This process of additive manufacturing uses sheets of material such as paper, or even metal to first create a compete layer of material over the whole build volume, and through subtractive manufacturing CNC or by other means remove the unneeded material [4].

These next series of additive manufacturing machines are used to print metal. Due to the research performed in this thesis, I had to choose which style of additive manufacturing would allow me to print copper with the greatest resolution. With that in mind availability of the machines to print the test specimen was another factor in choosing which machine was used in these tests [4].

Directed energy deposition is a method of additive manufacturing where the material being printed is either blown (if it is a powder), or extruded (if it is a wire) and uses a laser to melt the material as it is being placed into the voxel. Unlike the powder bed fusion method of additive manufacturing as discussed above which preheats a layer of powder material before final melting, the directed energy deposition method completely melts the material as it is being despotized [4].

Sheet Latinization is also one of the few ways in which metal can be printed today. As it was stated before, the sheets of metal are layered across the print volume and ultrasonically welded to the prior layers. By process of subtractive manufacturing, the unwanted voxels are removed to leave behind the desired layer. Copper can be printed in this fashion, along with few other metals [4].

Powder bed fusion is also another way to melt metal, and more specifically selective laser melting. By preheating the powder before melting only a small laser input is needed to fully push the powder voxels past their melting point and fuse to the surrounding voxels [4]. NASAs new series of rocket nozzles use this style of additive manufacturing to create the first full rocket engine. Marshalls Materials and Processing Laboratory, who printed the nozzle, fused 8,255 layers of copper to create the full scale part in 10 days and 18 hours [5].

Figure 1.4: Printed Copper Rocket Engine by Mashall Materials and Processing Laboratory

Interestingly enough the Materials engineers came to find the problems with printing high conductive materials such as copper and said post print: "Copper is extremely good at conducting heat," explained Zach Jones, the materials engineer who led the manufacturing at Marshall. "That's why copper is an ideal material for lining an engine combustion chamber and for other parts as well, but this property makes the additive manufacturing of copper challenging because the laser has difficulty continuously melting the copper powder." [5] Last for powder bed fusion is a process called electron beat melting, in this process a deflection coil electromagnetically moves the electron beam across the print volume instead of mirrors like in the select laser melting [4].

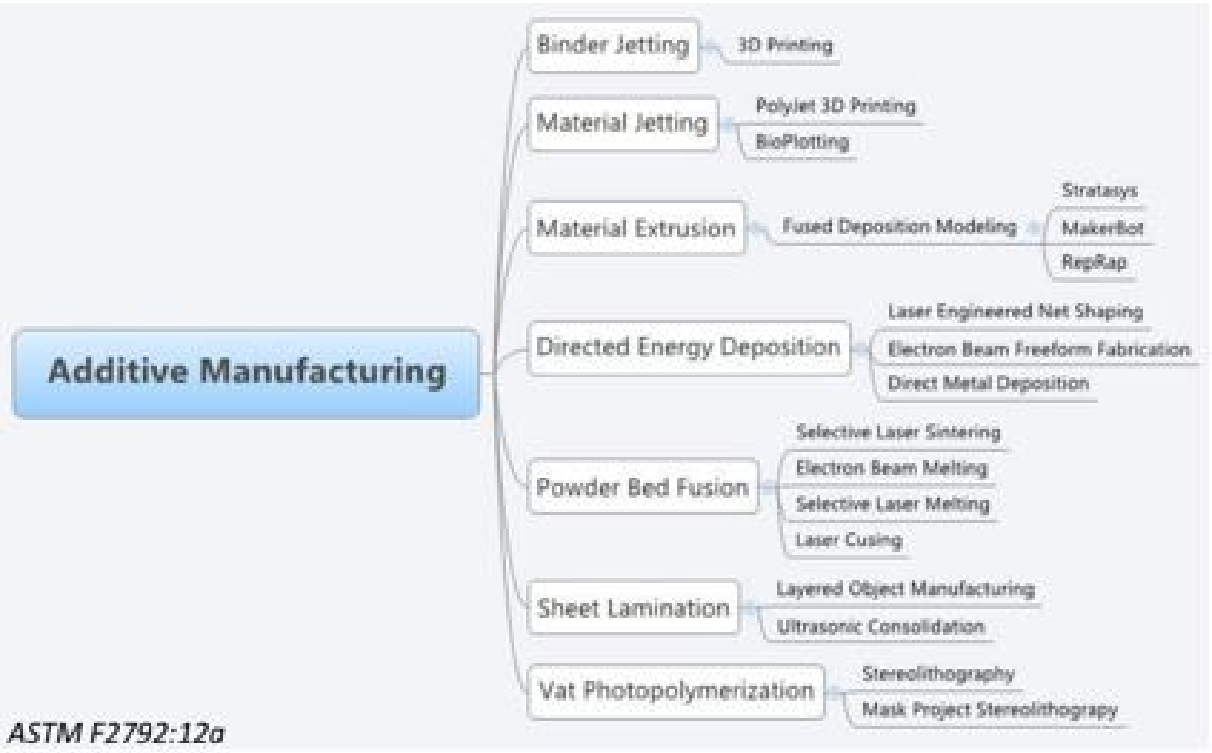

Figure 1.5: Figure showing the different methods of Additive Manufacturing

Seen in the figure above is a graph from the Additive Manufacturing Class slides taught by Dr. Christopher Williams at Virginia Tech. In the middle row are all the different styles of additive manufacturing with the next column of values to the right being the individual companies who make those specific style of Additive Manufacturing machines.

1.2 Binder Jet Printing

1.2.1 Problems with Printing Copper

The problem with the high thermal conductivity of the copper is keeping the energy to melt the powder inside the voxel. Due to the thermal conductivity of copper and other metals being so high, it is difficult to keep the energy from dissipating to other voxels on all sides. When more powder is melted outside the intended voxel it is called "print through." For most Metal printers having 100% density parts without this phenomena of print through is difficult to achieve. Therefore the last way to print metal without this phenomena of print through is called Binder Jetting [4].

1.2.2 How Binder Jet Printing Works

Binder Jetting is a way of additive manufacturing which has a series of steps to create high resolution metallic parts. Binder jetting has three steps to create a final part. First, the printer uses a series of inkjet heads and a linear actuator to print a "binder" or a glue to adhere the voxels together to create a parts called a green part. Post print, the part is put into a curing oven to cure the binder and increase the strength of the printed part. Last the cured green parts are placed into a kiln to be sintered into high density parts [4].

Due to the sintering of the powder only happening after all the support powder is removed from the part, and due the resolution of the binder printing head of the machine. This process of binder jetting produces very small parts with some of the best resolution of all the other prescribed metal printers. However this style of printing due to using a kiln to sinter the parts, and due to the infusion of binder spreading the copper powder apart before sintering, does not currently produce parts with 100% density [6].

1.2.3 Uses of Binder Jet Printing Copper

Currently in the manufacturing world there is an extreme variety of uses for copper due to the large thermal conductivity and also electrical conductivity. The properties of this metal allow the use of it in many electronic devices, and also in heat exchangers [6]. Currently in most lab tops and servers, heat pipes are used to wick away the heat from the CPU's which are placed in areas of low air flow. Electrically most of the wires and most devices within the power electronics area today are made with copper .

Therefore with additive manufacturing coming more and more prominent within the manufacturing scene, binder jetted copper will make its way into these rolls of transporting heat and electricity through most of our devices used today.

Due to the scalability of the binder jetting technology, larger machined objects will in time will also be created using this style of additive manufacturing. The problem as stated before with the other metal additive manufacturing techniques is the internal stresses constructed by the rapid heating and cooling of their parts from the lasers used to melt the powders. Because the only heat seen within the binder jet style of printing is the final sintering stage [7]. Mechanically the parts will perform better and have no warpage due to thermal stresses of printing. In the future, larger scale objects would be economically cheaper from "CNC"ing a large block of copper from only using the needed amount of material to fill the volume. The more complex the part, the more additive manufacturing will surpass any subtractive manufacturing method.

In the end, the future of binder jetted copper is as limitless as the current uses of copper is today. With the increase of complexity of personal electronic devices such as cell phones, and tablets increasing at the rate of Moore's law. With printed copper rocket nozzles being used in space current space applications, and with the Wendelstein 7-X fusion reactor having their first successful test fire this year, who knows where the application of complex copper parts will be needed. Overall, there is only one technology which can keep up and produce the ever increasing complexity of these parts, and that would be binder jet printing.

1.3 Thesis Overview

As has been stated prior within this thesis, Binder Jet Printing due to the steps of how a part is made, the resolution of the printed part is captured within the first process of binding all the powder together creating the green part. However this unique byproduct of having high resolution prints comes at a cost both thermodynamically and electrically due to the porosity of the part. Besides NASA back in 1971 [8] who researched compressed sintered powders, no research has been performed to find the thermodynamic and electrical conductivities of Binder Jetted Copper.

Therefore the two questions which will be answered in this thesis will be:

- "Is there a relationship between density of binder jetted copper and the overall Lorenz number of the metal?"
- "If so, can a mathematical equation be created to allow for more precise use of the Wiedemann Franz Law within Additive Manufacturing?"

To fully understand the scope of the problem a basic history and theory of all parts of the Wiedemann-Franz law needs to be given. So in this thesis you will first read the history and theory of how both thermal and electrical conductivities came to be what they are today. Then, the history and application of the Wiedemann Franz Law will conducted to show the linking of both electrical and thermodynamic conductivities. Next, this thesis will go over the methods of finding both the thermodynamic and electrical conductivities of a material. Followed by the test procedures of both the electrical four wire testing, and the laser flash method. With last but not least, the results and conclusion of this thesis will be shown and stated.

The purpose of this thesis is to show how the density of binder printed copper will change the thermodynamic and electrical conductivity of the metal. With the decrease in density the overall thermal conductivity of the metal will decrease, and the density change will increase the electrical resistance, overall changing the Lorenz number. This thesis will therefore add a density term to the calculation of the Lorenz number. Future tests will hopefully test the correlation curves found in this research to that of other metal powders and alloys.

Chapter 2

Background

2.1 History of Electrical Conductivity

Electrical Conductivity is one of the main components of the Wiedemann Franz law and must be understood. Electrical resistivity which is the inverse of electrical conduction and was discovered by Georg Ohm in 1827. The ratio of voltage divided by current is also called the chordal resistance. His original Equation 2.1 can be seen below [9]:

$$V = I * R \tag{2.1}$$

- R = Resistance measured in ohms.
- V = Voltage potential across the object measured in Volts.
- I = the current through the object measured in Amps.

Direct Current (DC) resistance is the type of resistance which will be detected through the test specimens, and will vary with the length of the test specimen. There is therefore a difference in the terms Resistance and Electrical Resistivity. Electrical Resistivity, which is also called "specific electrical resistance" is measured in Ω * meters. And the relation of Electrical Resistivity to resistance, length, and diameter of the test specimen can be seen in Equation 3.1 below [10].

$$R = \left(\frac{\rho L}{A}\right) \tag{2.2}$$

- R = Resistance measured in Ω
- l = length of the test specimen in meters
- σ = electrical resistivity measured in $\Omega \cdot meters$
- A = cross sectional area of the test specimen

In room temperature, most of the resistance seen in a metal specimen is due to the scattering of electrons from thermal vibrations within the metal. The sea of electrons therefore do not have a straight path to the opposite side of the metal piece, and therefore interact with each atom causing more thermal vibrations. When current is applied to a metal with resistance, it will heat up over time. If the thermal dissipation of the metal is equal to the overall electrical dissipation within the metal a steady state temperature is reached. This is also the reason different gauge wires are recommended for different currents [11].

Cooling and heating the metal will change the electrical resistance of the material due to the increased and decreased thermal vibrations within the atomic lattice structure. If cooled past the Critical Temperature, metals will go into a superconducting state, and in this state the resistance of the material virtually drops to 0 [11].

Materials above their Critical Temperature will have a linear resistivity drop due to the Pauli Exclusion Principle, which states two electrons cannot have identical quantum numbers [12]. This principal applies to photons (single particles) and not bosons (pairs of particles) which means when the internal energy within the material drops below the bonding energy for Cooper pairs ,which is 10ˆ–3 eV, Electrons will form a Cooper Pair [13]. When the electrons are in a Cooper Pair they can pass through the lattice of atoms at the same energy states unhindered, and therefore the overall resistance of the material become 0 ohms [11].

2.2 History of Thermodynamics

The Greeks originally thought the classical five elements where fire, water, wind, earth, and aether [14]. The ancient Chinese thought the elements were wood, water, fire, metal, and

earth. The Japanese had the same elements as the ancient Greeks with the exception of using the term "void" for aether [15]. Even up to the medieval times, Sulphur, Mercury, and Salt [16] were the only additions to the original five elements taught by the ancient Greeks [17].

All of the ancient cultures as seen by their elements realized fire was an important part of the building blocks of the universe. Undenounced to everyone until the age of enlightenment, fire, which became "heat" and later Thermodynamics proves that all the ancient minds were correct at assuming energy is important to know and understand! The study of thermodynamics lets us as scientists and engineers understand the energy transfer throughout mechanical, chemical, and atomic processes of every system within the known universe.

The change from the classical elemental theology to concrete science started in 1840–1850 by James Joule [18]. By showing through experimental means to the academic community James Joule showed that heat was not a fluid-like substance, and is actually a form of energy. Sadi Carnot also had a few notions on the true relation of heat and energy when discovering the ideal engine in 1824 [18]. Also in the same time period of James Joule, Rudolf Clausius and William Thomson (1st Baron Kelvin) both stated the first law of thermodynamics, "Total energy has to be conserved," and the second law of thermodynamics "Entropy of a system must increase, or in an ideal system remain constant." [18]

Today thermodynamics as defined by Merriam- Webster has become "the physics that deals with the mechanical action or relations of heat."

2.3 Testing Methods For Electrical Conductivity

For testing the resistance of a resistor, calculating the differential voltage of two points on a circuit, or even finding the current within a circuit is easy if the values are within the operating range of a standard multimeter. However when the resistance of the test specimen is smaller than the resistance of the wires used to find the resistance, it is hard to find the exact value due to the huge error induced by the equipment itself [19]. This paradigm of finding the resistance of an object without changing the value is like Schrodinger's Cat example used in physics. The two major ways everyone today is calculating the resistance of specimens are 2 wire and 4 wire methods [19]. Both of these methods use ohms law to calculate resistance. Dependent on the method either the multimeter or an outside power

supply supplies the current, and the voltmeter built within the multi meter or external voltmeter will calculate the resistance.

The 2 wire method, or simply using an ohm meter is a method of calculating resistance of a test specimen by connecting only two leads on either end of the object. However by having both the current and voltage measurement occurring on the same lines, the resistance of the wires plays a huge factor in the error within the electrical system [19].

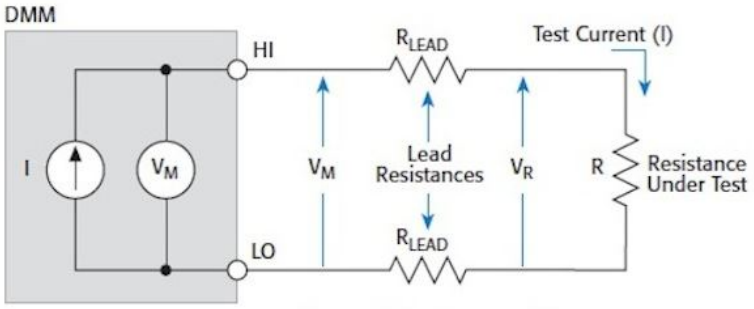

Figure 2.1: Diagram of the 2 wire resistance measurement

Above is a figure showing the electrical diagram of the 2 wire method [19]. In this diagram the gray box is the multimeter which contains both the voltage measurement and current source. As seen Vm is calculated at the high and low pins of the multimeter, and not at the test specimen labeled R [19].

Also it can be seen in Figure 2.1 that the two wire method uses a current source and voltage measurement circuit within the multimeter. As can also be seen in the figure above, the resistance under test has the lead resistances interfering with the resistance measurement. Therefore the equation to use this style of measurement is as follows [19].

$$MeasuredResistance = \frac{V_m}{I} = R + (2 \cdot R_{Lead}) \tag{2.3}$$

- V_m = Voltage measured at the meter.
- I = Current supplied by multimeter.
- R_{Lead} = the resistance of the leads from the multimeter to the resistor under test.
- R = Resistance under test.

If the resistance in the wires is not taken into account then the value obtained by the voltmeter in the multimeter will be too high, and a larger resistance will be observed. Also due to the current source unable to source a large current and voltmeter unable to detect small voltages, this style of measurement is usually limited to the specs of the meter. The Fluke 80 Series 87–5 multimeter for example has an error within its probes of 0.1 – 0.2 ohms [20]. For measuring a resistance of .001 or less ohms the 4 wire method will have to be used [20].

The second style of measuring resistances is the 4 wire method. is similar to the 2 wire method in such that there is a current source and a voltmeter. However, in the 4 wire method the current source and the voltage source are 2 separate machines and the voltage sensing lines are separate from the current supply lines. Seen in the figure below is a schematic of how the 4 wire method is constructed [19]. As can be seen in Figure 2.2, the sense lines and source lines are completely separate, and therefore the voltage measured across Vm is generally thought as the correct values [19].

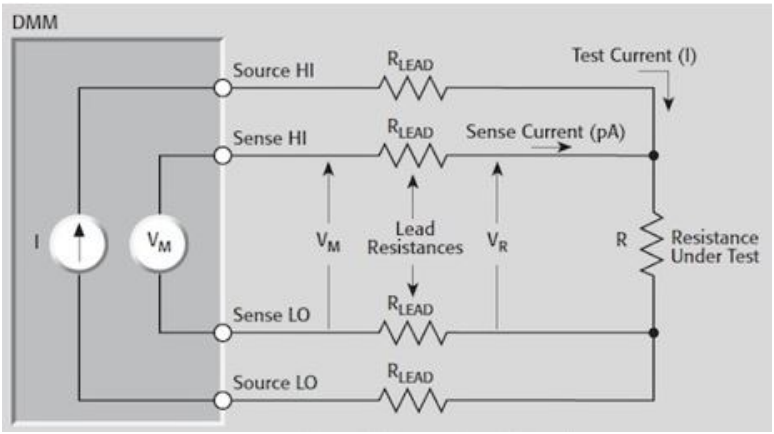

Figure 2.2: Schematic of how the 4 wire method is performed.

However in Figure 2.2, there are still resistances associated with the 4 wire method. However as seen in the figure, the picoamps associated with finding the voltage across R is generally ignored, and the Voltage measurement is thought of as correct [19]. Using this style of measurement, the current source and voltage measurement meters can be chosen with the correct specifications. If the four wire method is used by the Rigol DM3068 the minimum resistance which can be detected is 200.0000 ohms [21]. So with the 6 1/2 order of magnitude of resolution the 200 ohm setting can accurately detect 0.003 ohms [21].

Sadly from the calculations of the BJC rod geometry, the expected value for the resistance

was close to 0.0014 ohms. Due to the Rigol DM3068 not having the resolution needed to detect such low ohms, a larger current source was chosen, and through ohms law in Equation 2.1, the meter would only need to read voltage. Therefore to find the milliohm resistances, a current source of 10 amps can be chosen, and a voltmeter would only have to measure 10 mV, which for the Rigol DM3068 is well within its range.

2.4 Testing Methods for Thermal Conductivity

To find the thermodynamic conductivity of a material there are several different types of methods. As seen in this section, all of the different methods have different ranges of thermal conductivity in which they can measure. Besides just the range of thermal conductivity the machines also have different temperature ranges in which they can calculate the thermal conductivity, but due to all machines being able to calculate values at room temperature, this specification does not matter. The first machine for thermal conductivity is the guarded hot plate method, and it is one of the oldest and most trusted sources of figuring out the thermal conduction coefficient for insulators. For this method to work, a solid sample must be machined carefully to decrease the amount of air gaps between the hot and cold plates which are above and below the sample being tested. Any air gaps will increase the thermal resistance of the interface and need to be minimalized as much as possible for the measurement to be more accurate. Thermal paste can be used to minimalize the amount of thermal resistance but a machined interface is more preferable [22].

Calculations for this style of thermodynamic measurement include measuring the distance between the hot and cooling plate seen in Figure 2.3. The temperature gradient is then calculated using thermocouples and the thermodynamic conduction coefficient is calculated using the distance between the plates and delta T [22].

Used mostly for insulators and can detect below 0.1 W/m*K. This method is not good for detecting the thermal resistance of liquids or high conductivity metals [22].

The transient plane Source seen in Figure 2.4 uses a nickel sensor which is covered with insulating material Kapton. The sensor is placed between two identical samples. Current is sent to the nickel sensor and heated. The temperature vs. time data is then converted to a thermal conductivity coefficient. A more detailed report of the transient plane source can be found in the ASTM manual [23].

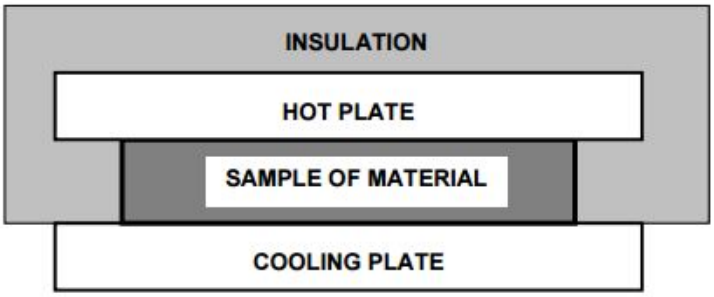

Figure 2.3: Guarded hot plate method schematic

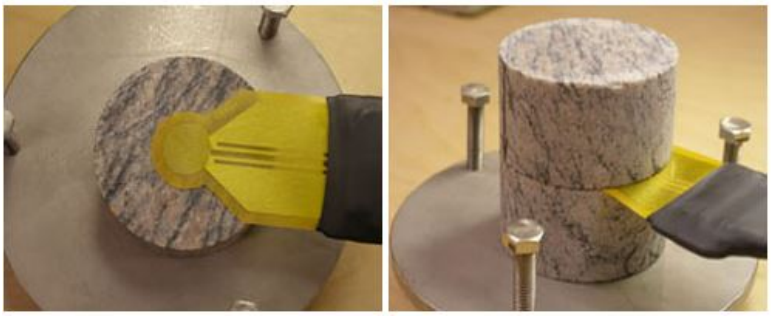

Figure 2.4: Transient Plane Source method photos

The modified transient plane source, seen in Figure 2.5 uses a heat reflectance sensor which is supported on an insulated backing and surrounded by a guarding ring for only one dimensional heat flow. There is a voltage sensor which is calibrated for temperature. The rise in temperature is inversely proportional to the thermal conductivity of the material. The more heat which is defused throughout the sample is directly correlated to the increase in thermal conductivity. In Figure 2.6 the inverse effect of the voltage and correlated temperature increase for insulative materials such as foam, or conductive materials such as metal can be seen [24].

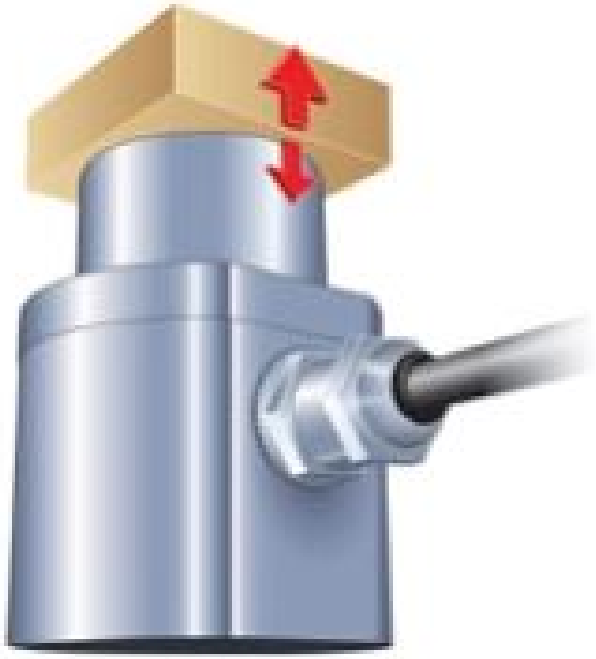

Figure 2.5: Modified Transient Plane Source

Laser Flash Diffusivity is a thermal conduction measurement method which uses a laser to flash one side of the test sample, usually only 1cm^2 face with only 1mm thickness, and has an IR sensor on the back side to calculate the temperature rise. The resultant temperature rise on the opposite side of the specimen is recorded with an inferred sensor as a function of time, and all associated variables are calculated from the Temperature Vs. Time graph [25].

This is a figure showing how the T1/2 is calculated from the Temperature VS. Time graph from the laser diffusivity measurements. Once the value of alpha is calculated using the

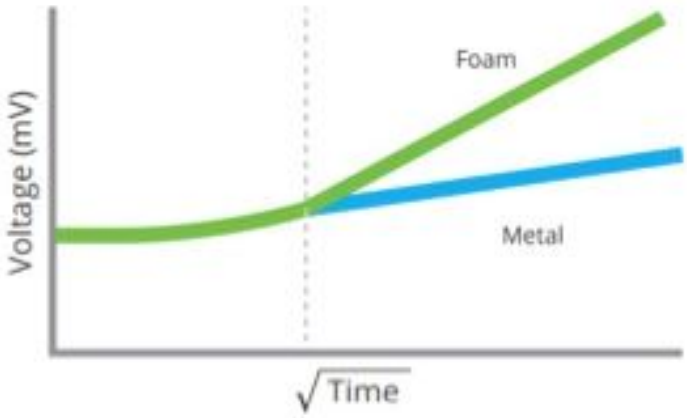

Figure 2.6: Time Vs. Voltage Graph from the Modified Transient Plane Source

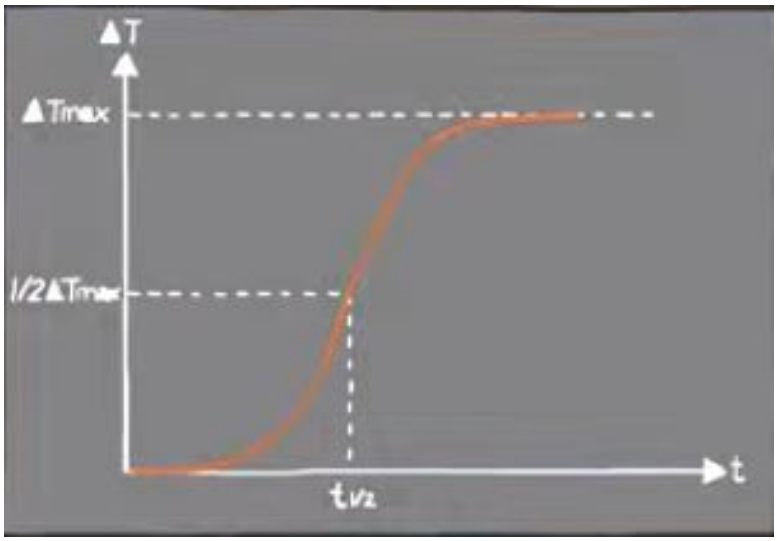

Figure 2.7: temperature Vs. Time graph from a Laser Diffusivity Machine

thickness of the sample, and the T1/2 data. the thermal conductivity can be calculated with the Cp value [25].

To calculate the Cp value the temperature Vs. Time graph as seen in Figure 2.7 is taken, and a delta T is calculated for a regulated time amount. This delta T value is placed into Equation 2.5 with the mass of the test specimen and Cp is calculated by comparison with Cp values from a sapphire calibration disk. Therefore dependent upon the temperature and thermal conduction range needed for the sample, one of the four methods below are used to determine the thermal conductivity of the material [25].

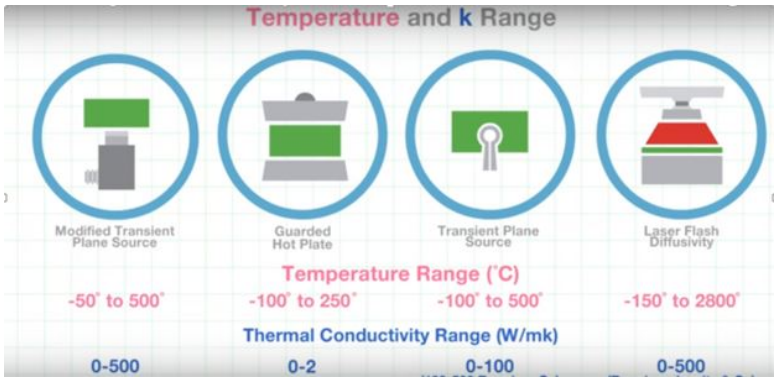

Figure 2.8: the thermal conductivity ranges of the different methods of thermal measurement

It is highly important that the thermal conduction range for each of the different methods is stated, because only two of the above methods can handle the high conductivity of copper. The Modified Transient Plane Source method can calculate thermal conductivities between 0 - 500 W/mK [24]. The Guarded Hot Plate can only calculate between 0–2 W/mK [22]. The Transient Plane Source between 0–100 W/mK [23]. And last the Laser Flash Diffusivity between 0–500 W/mK [25].

After looking at the data shown in Figure 2.8, to measure a value of thermal conductivity in the range of 200 – 400 W/mK, only the modified transient plane source, and the laser flash diffusivity machine will work. However because Dr. Scott Huxtable has a laser flash diffusivity machine which is available to use, the thermal conduction measurements will be conducted on his machine.

The laser flash method uses a comparative method find the specific heat of a sample as can be seen in Equation 2.5. When the machine is calibrated using the sapphire calibration disk, the temperature rise and other associated data for the sapphire sample is stored. Assuming

the laser pulse and other environmental factors do not change between samples, Equation 2.5 can be used to find the Cp for the sample.

$$C_p = \frac{Q}{m \cdot \Delta T} \tag{2.4}$$

- C_p = specific heat.
- m = mass.
- ΔT= change in temperature.
- Q = energy.

$$C_{p(sample)} = \frac{mC_p\Delta T}{m\Delta T_(Sample)} \tag{2.5}$$

- C_p = specific heat.
- m = mass.
- ΔT= change in temperature.

After the Cp values have been found from testing, the t1/2 value can be found from finding the time it takes to reach half of the maximum temperature. After finding the thickness of the sample, the thermal diffusivity (α) can be found. Now using Equation 2.7 [26], the specific heat, thermal diffusivity, and density values can be used to find the thermal conductivity (K).

$$\alpha = 0.1388 \cdot \frac{d^2}{t_(1/2)} \tag{2.6}$$

- α = thermal diffusivity
- d = thickness of the sample
- $T_(1/2)$ = is the time to the half maximum

$$\alpha = \frac{k}{\rho \cdot C_p} \tag{2.7}$$

- α = thermal diffusivity
- k = thermal conductivity
- ρ = density
- C_p = specific heat capacity

2.5 History of the Wiedemann Franz Law

The law was named after the two physicists Gustav Heinrich Wiedemann , and Rudolph Franz, who collaborated in 1853 to create the Wiedemann –Franz law. The Law back in 1853 only empirically related the thermal conductivity and electrical conductivity of any metal to a constant number at the same temperature. Below is the Equation 2.8 [27] from 1853 [28].

$$\frac{K}{\sigma} = L \cdot T \tag{2.8}$$

- K = Thermal Conduction Coefficient
- σ = electrical conduction coefficient
- L = Constant = $2.45e^{-}8W\Omega/K^2$
- T = Temperature in Kelvin

Ludvig Lorenz was a mathematician and physicist who discovered in 1872 the proportionality of K/σ with temperature. Due to his discovery the constant term above "L" became the Lorenz number.

2.6 Theory of the Wiedemann Franz Law

The whole theory of the Wiedemann Franz Law is based off of the coincidence that electrical and Thermal Conductivity uses metallic bonding and free electrons in the material to transport the energy. Any material such as wood, metal, and even polymers are made of atoms and the forces of attraction between these atoms are called chemical bonds. The type of chemical bond is dependent on the atomic properties of the molecule. The common types of bonds are Ionic, Covalent, and polar covalent bonds [29].

In a Covalent bond there are shared electrons between two atoms, in an ionic bond an atom seals an electron from another atom creating a positive and negative charged atomic pair. A polar covalent bond is a particular type of covalent bond where the resultant molecule has its shared electrons spend more time on one side of the molecule. As resultant, the whole molecule becomes positively and negatively charged on opposite sides. Diagrams of these different types of atomic bonds can be seen in Figure 2.9 [29].

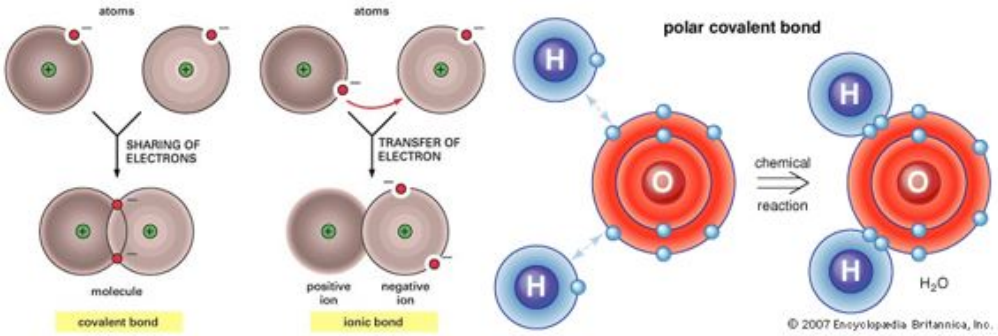

Figure 2.9: The different types atomic bonds.

The last type of bonding within materials is called metallic bonds, and can be seen in Figure 2.10. These types of bonds are different from the other three and can best be described through the "electron sea" model. In this model all the atoms are within a crystalline structure, and due to the very weak attraction force from metals outer valence electrons, the electrons will break away from their host and freely move between all the positively charged atoms. This "Sea" of electrons is the only force holding the positively charged cations together. Consequently due to these valence electrons freely floating throughout the metal, the electric conductivity and thermal conductivity of metal is high compared to other materials with different bond types [29].

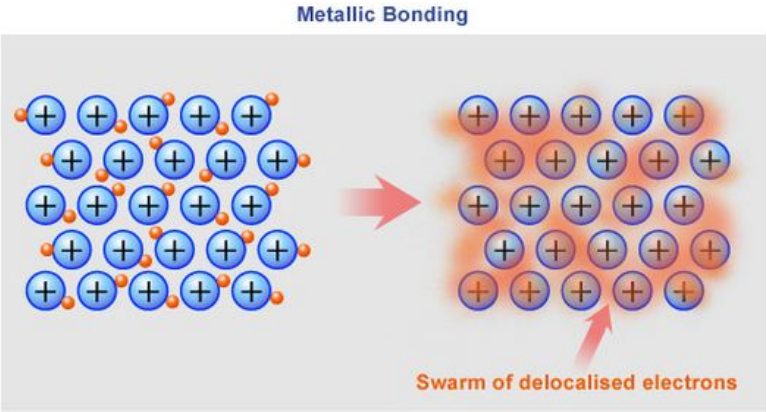

Figure 2.10: Metalic Bonding Schematic

On the periodic table the group 11 elements which are copper, silver, and gold have only one valence electron in their outermost electron ring. This can be seen in the electron diagram of these elements in Figure 2.11 [30]. Only having one valence electron in the outer ring gives a very weak attraction force to the cations, and gives this group a very high thermal conduction coefficients, and electrical conductivity. Today gold, silver, and copper, are used in thermal and electrical systems due to these characteristics [29].

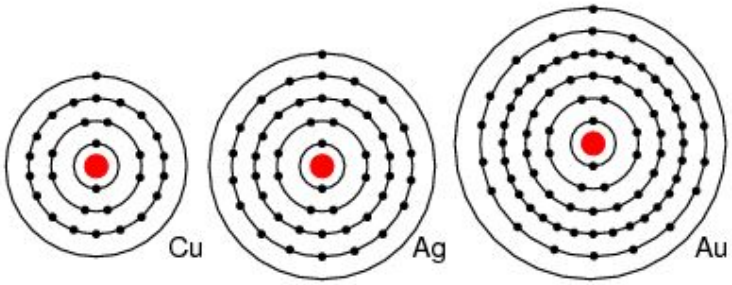

Figure 2.11: The electron configuration of Copper, Silver, and Gold respectfully from left to right.

As discussed before the electrons can best be best described as being in a "Sea" and freely flowing between all of the cations of the metal. Interestingly enough because of this effect, the Wiedemann Franz Law can be understood by treating the electrons like a classical gas [29]. With this idea in mind the equations for thermal and electrical conduction now become:

$$K = \frac{n\langle v\rangle \lambda k}{2} \tag{2.9}$$

- n = particles per unit volume
- $\langle v \rangle$ = Mean particle speed
- λ = Mean free path
- K = thermal conductivity

$$\sigma = \frac{ne^2\lambda}{m\langle v \rangle} \tag{2.10}$$

- n = particles per unit volume
- λ = Mean free path
- $\langle v \rangle$ = Mean particle speed
- σ = electrical conductivity

$$\langle v \rangle = \sqrt[2]{\frac{8KT}{\pi m}} \tag{2.11}$$

- $\langle v \rangle$ = Mean Particle Speed
- K = Thermal Conductivity
- T = Temperature in Kelvin

After the Quantum mechanical treatment has been performed on the equation it becomes:

$$L = \frac{k}{\sigma \cdot T} = \frac{\pi^2 \cdot K^2}{3e^2} \tag{2.12}$$

- K = Thermal Conductivity
- T = Temperature in Kelvin
- σ = electrical conduction
- L = Lorenz number

This is the equation which is used today for calculating the thermal and electrical conductivities of a metal. Experiments have shown the Lorenz number for copper is $2.23 \cdot 10\hat{}{-8}$ $W\Omega/K^2$ at 273K and $2.33 \cdot 10\hat{}{-8}$ $W\Omega/K^2$ at 373K [29].

However binder jetting copper will not allow for a 100% dense metallic structure [31].

Even though there is still a "Sea" of electrons throughout the part, the pockets of air, argon, or hydrogen from the sintering process of the binder jetting will interfere with the means free path between two points in the metal. Virtually the voids increase the distance of electrons between the two points to increase the distance in the electrical resistivity measurement, but the voids create pockets of convection within the metallic piece. These voids create an overall thermal resistance. The questions answered in these sets of experiments becomes, "Does the thermal conduction change at the same rate of the electrical conduction?" If the rate of change differs in either the thermal or electrical conduction values, the overall Lorenz number will have to change. This research will model that change with the density values of the printed copper.

Chapter 3

Creating Test Specimens

To create the test pieces used within the sets of experiments, there are a few different needed to be understood before sending the .STL files to be printed. The design challenges which would need to be designed around were:

- The extremely high electrical resistivity of copper 1.68e-8 $\Omega \cdot m$
- Limited space in the thermal test device volume
- Shrinkage of the copper parts by 15 - 20 percent post sintering.
- Fragile nature of the green parts post sintering.
- High thermal conductivity of the copper pieces 385 W/mK

Both the electrical resistivity measurements and thermal conductivity measurements forced the design of the test specimens, and therefore the shape of the thermal test specimen was a 1.2 cm disk with a height of only 1.2mm. Difficulty of keeping the fragile green and green disks from breaking, was a challenge but through using the tools seen in Figure 3.5 it was all possible. The 2mm thick disks seen printed alongside the 1.2 mm disks where printed as a precautionary measure just in case the 1.2mm disks were too fragile. Due to prior experiments completed by Yun Bai at Virginia Tech [31] [6], it is understood that for a 85% density sintering profile described in Figure 3.9 and Figure 3.10 a 15–20% shrinkage of the parts is expected. Overall this will create 1cm by 1mm sintered parts to be used in the laser flash rig [31].

The second batch of binder printed copper disks were printed with the same geometry and with the same saturation. The sinter profile for the second batch of copper disks can be seen in in Figure 3.10.

The third batch of copper specimens that were printed used bi-modal powder. Instead of the uniform 15 micron powder used in the first and second batches, a homogeneous mixture of 30 and 5 micron powder was used. The disks where printed assuming 18% x and y plane shrinkage and 16% z axis shrinkage. The sintering profile for the third batch of specimens was tailored for maximized density. Therefore the temperature was increased to 1075 degrees Celsius just as it was in the second batch of test specemins. The time at temperature was also increased to 180 minutes at sintering temperature [6].

Electrically in order to increase the resistance of the test specimens a thin rod was designed. Due to Equation 3.1 [10] seen before in the theory section :

$$R = \left(\frac{\rho L}{A}\right) \tag{3.1}$$

- R = Resistance measured in ω
- l = length of the test specimen in meters
- σ = electrical resistivity measured in $\omega \cdot meters$
- A = cross sectional area of the test specimen

To increase the resistance of the object, the length of the test specimen must be maximized, at the same time the cross sectional area of the test specimen must be decreased as much as possible. Too thin of a rod will break on transport and will not survive the added pressure of the gator clips used to attach the rods to the 4 wire method. Therefore a 2mm diameter by 180mm rod was designed, and sintered to create a 1.9mm by 154mm sintered rods.

For the third batch test specimen geometry was changed due to the smaller size of the print piston. The diameter of the rods was kept at 2mm, however due to a 55mm x 45mm print plane the geometry was changed from a straight rod to a U shape. This geometry increased the distance between the voltage probes to about 100mm.

The powder used in all of the experimental specimens was from AcuPowder. The single mode powder used in the first and second batch was the 500A ultra-fine atomized copper

powder with median particle size of 15 micron. The bimodal powder used in the third batch was 30 micron (w.t.73%) + 5 micron powder.

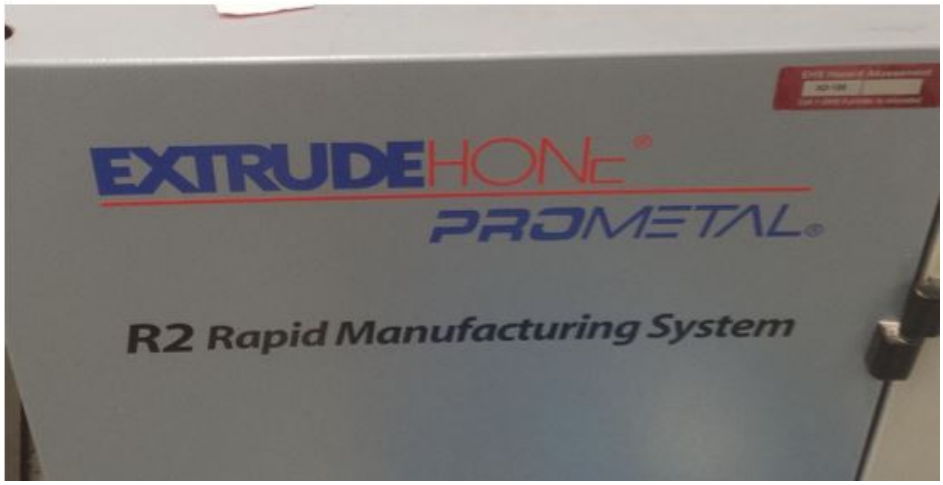

Figure 3.1: This is the printer used to binder jet the test samples for the thermal and resistance test.

Seen in Figure 3.2 is the binder jet printer used for creating the test specimens. The overall print required 54 layers and a print time of only 1 hour 30 minutes. Saturation of the print was set to 100%. The heads of the printer were clogged halfway through the print and were cleaned. The overprint can be seen in Figure 3.4.

To cure the parts from printed to green parts, usually the whole build tray would be placed into an oven overnight to cure the binder. However due to the small volume of the print it was opted to let the IR heaters continue to run for two hours and let set overnight.

It was highly important when removing the test disks and rods from the powder bed that all the residual powder was removed. For the test disks to seat properly within the laser flash diffusivity machine the surface of the disks had to be free of powder clumps caused by static electricity. Only when the green parts left the powder bed could the cleaning process happen simply because after the sintering of the disks, any loose attached powder will sinter to the disks. Seen in Figure 3.5 are some of the dry paint brushes which were used to lightly dust off the residual powder clinging to the disks.

When removing the disks from the powder bed, the first batch of parts started to crumble when the tweezers where used, and therefore for the second batch of disks and rods my fingers where used to transport and manipulate the test specimens.

Figure 3.2: The Binder jet printer used to print the test samples.

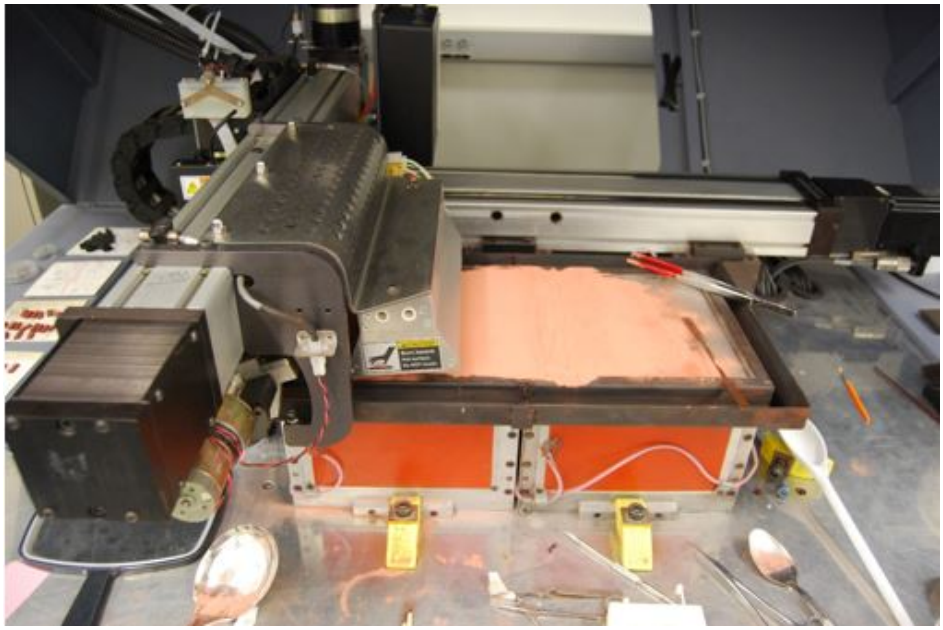

Figure 3.3: A photo of the printer, build tray, binder print head, and powder spreader.

Figure 3.4: This is a photo of a clogged print head over placing binder in the 15 micron powder.

Figure 3.5: The instruments used to manipulate the test specimens to the ceramic kiln trays.

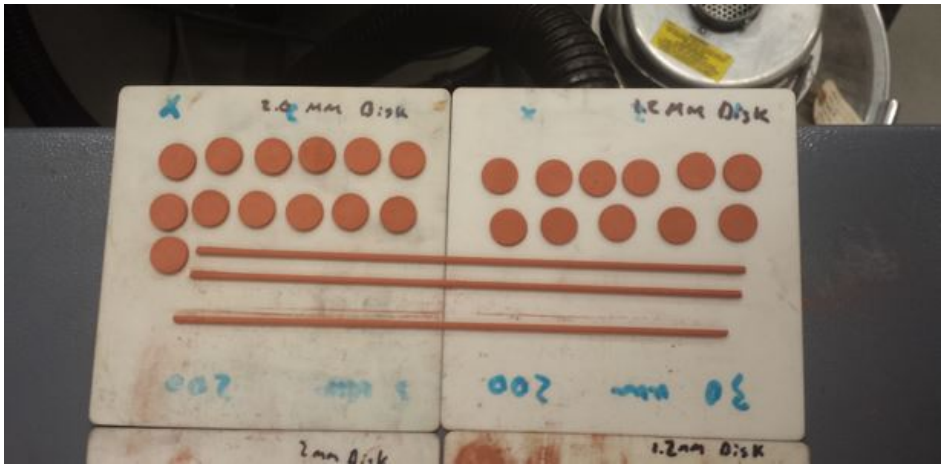

Figure 3.6: This is the test specimens after binder jetting.

After the parts were moved to the clean ceramic build trays they were placed inside the sintering kiln. Before the parts were sintered, the whole kiln was flushed at 20 liters per min with Argon gas for 10 minutes. Next a hydrogen supply of 5–6 liters per min was used to increase the temperature to 450 degrees C at a rate of 5 degrees C per min. A temperature of 450 degrees C was held for 30 minutes to burn off all the binder within the test specimens. A second temperature increase to 1070 degrees C was then performed at an increase of 5 C per min. 1070 degrees C was held for 2 hours and this temperature is where the sintering of the copper occurred. 1070 was used instead of the recommended 1080 due to the error variation within the internal temperature sensors. Any temperature above 1085 will burn and not sinter the parts overall ruining the test specimen. Therefore to play it safe a temperature of 1070 degrees C was chosen. Figure 3.9 shows the temperature Vs. Time graph described in this paragraph. Total time in the kiln was over 500 minutes.

The second batch of binder printed copper disks were printed with the same sinter profile as before with the exception of the maximum temperature being changed from 1070 to 1075, and the peak temperature time being extended from 2 hours to 3 hours. The overall result of these two changes will increase the density of the prints and will give me more points for the correlation equations. The time verses temperature profile for the second batch of test specimens can be seen in Figure 3.10.

Due to the control scheme of the Extrude Prometal kin, there was a 10 degree C overshoot in the temperature when rising to the sintering temperature, and therefore to not burn the parts at 1090 the second sintering temperature of 1075 was chosen instead of 1080.

The third and final batch of copper parts where flushed with nitrogen instead of argon. The resultant copper pieces post sintering had a shiny copper color instead of the normal flat orange color seen in the other figures. But the difference in color could also be attributed to the high 92% density from both changing to bi-modal powder and longer sintering profile.

Figure 3.7: This is a photo of the kiln used to sinter the printed copper.

Seen in Figure 3.11 are the finished test pieces used in the experiments to find the Lorenz number for binder jetted copper. The 1.2mm thick disks where used to find the density of the copper printed pieces.

Figure 3.8: The hydrogen and argon gas bottles and regulators used to supply the kiln to sinter the binder jetted pieces.

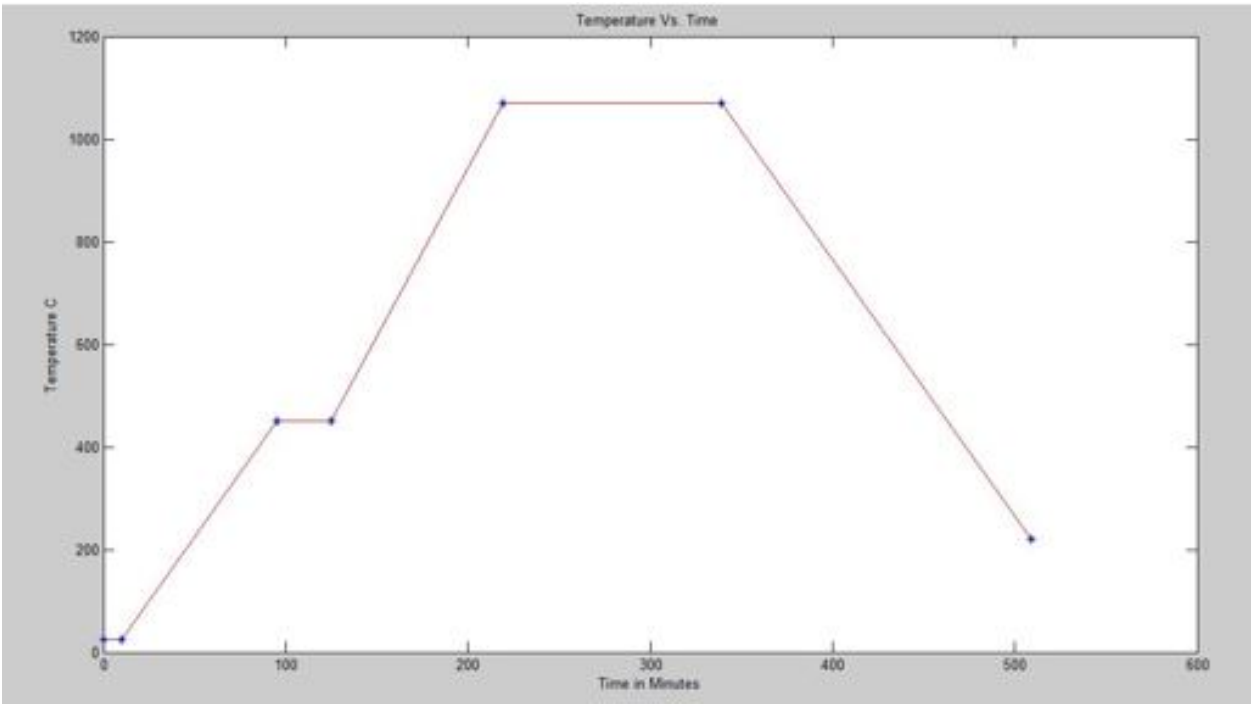

Figure 3.9: This is the temperature and time data of the sintering profile for the first batch copper test specimens.

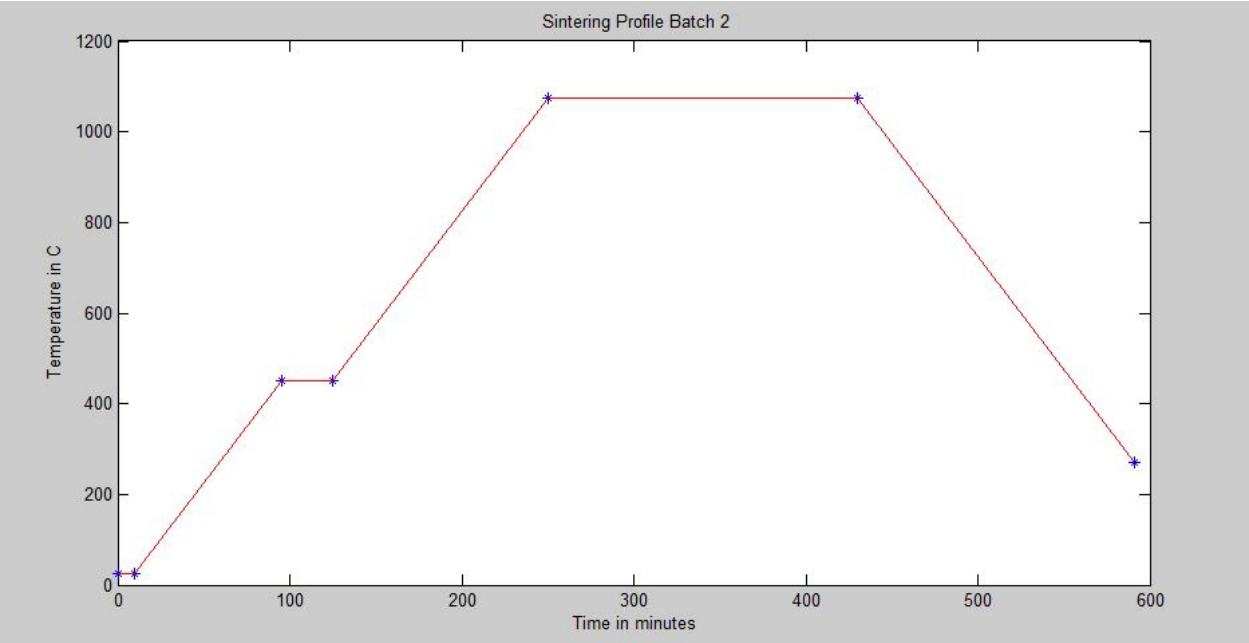

Figure 3.10: This is the temperature and time data of the sintering profile for the second and third batch of copper test specimens.

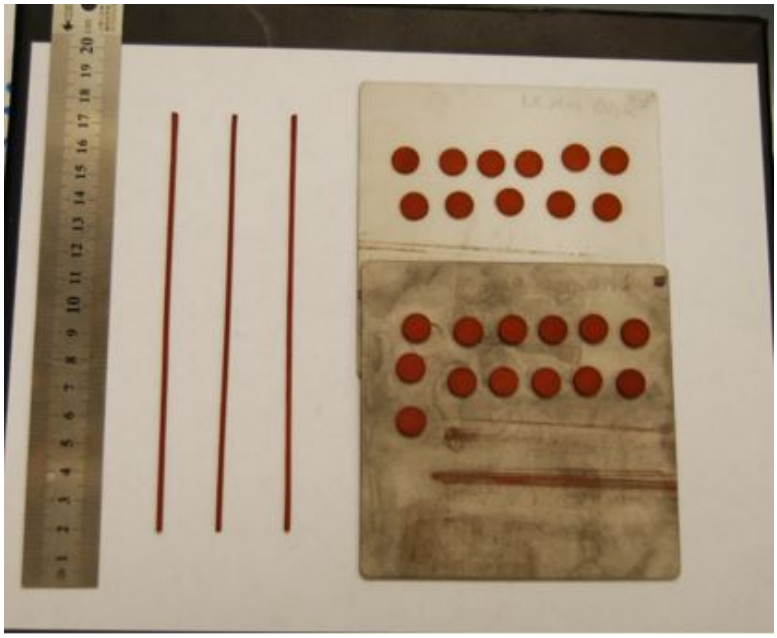

Figure 3.11: A photo of the Binder jetted specimens after sintering. The ruler shown is in centimeters.

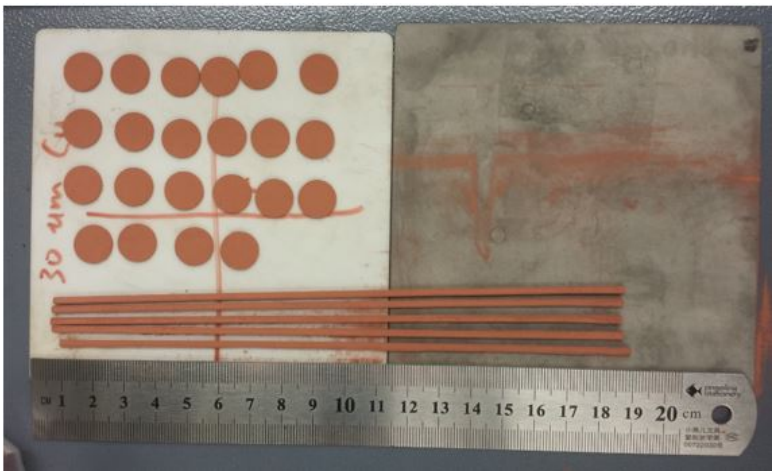

Figure 3.12: This is a photo of the second batch of test specimens before sintering.

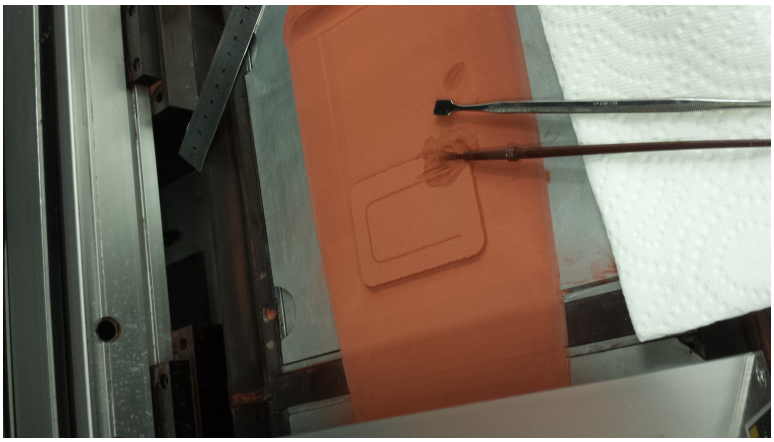

Figure 3.13: Photo of the third batch of electrical resistance copper specemins.

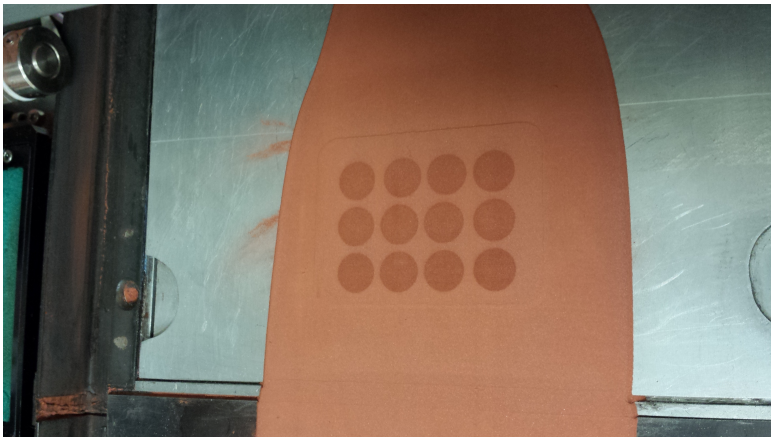

Figure 3.14: Photo of the third batch of thermal conductivity copper test specemins.

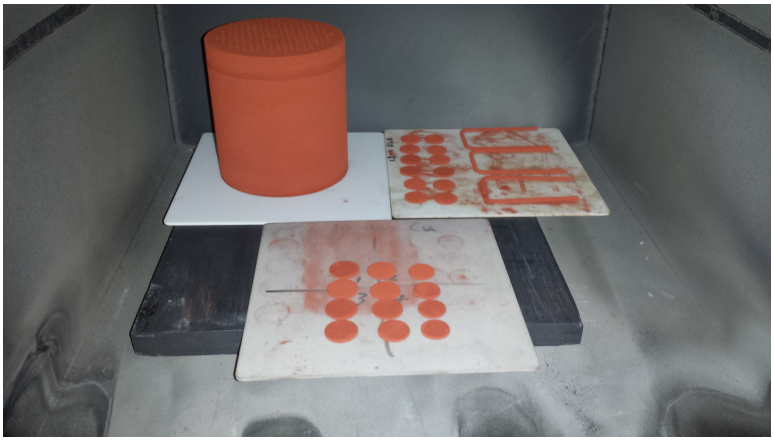

Figure 3.15: Photo of the third batch copper test specimens in their orientation within the kiln.

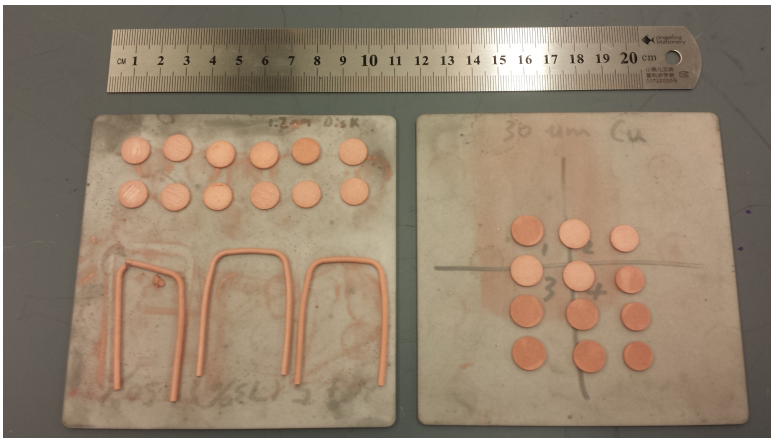

Figure 3.16: Photo of the third batch copper test specimens post kiln.

Chapter 4

Electrical Resistance Test Plan

To measure the electrical resistance of the binder jetted sintered copper rod, the four wire resistance measurement method was used. The measurement consists of separating the current and voltage measurements to two separate meters, and therefore not allowing the current flow from the ammeter to interfere with the voltage measurement of the Voltmeter. Using Ohms Law to reverse calculate the resistance of the test specimen is just the Voltage measurement divided over the ammeter measurement. Below is the schematic of how the voltage and ammeter measurement equipment was connected to calculate the specimen resistance.

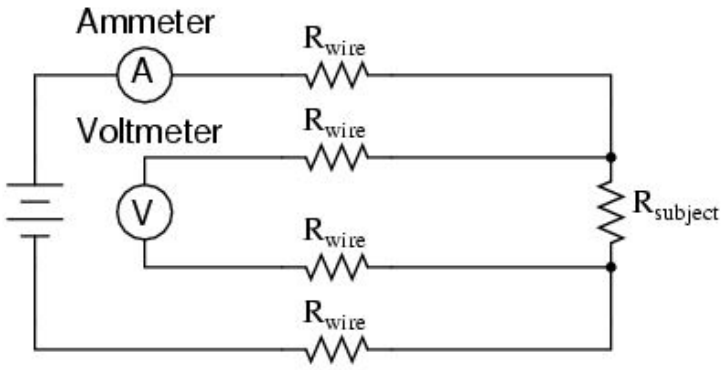

Figure 4.1: Schematic showing how the voltmeter and ammeter was connected to the test specimen.

The current source for this measurement was a 10 amp Agilest E3633A. 10 amps were used to calculate the resistance of the test specimen.

Figure 4.2: This is the Agilest E3633A ammeter, which was used to supply 10 Amps to the test specimen.

For this four wire resistance measurement to be able to measure the low resistance of the test specimen, the Rigol DM3068 was needed to calculate the voltage drop over the rod. Below in Figure 4.3 is the high end multi meter needed for the measurement. The Rigol DM3068 was used as the Voltmeter to calculate the voltage differential in the copper rod due to its 6.5 digits resolution. As can be seen in Figure 4.3 the Rigol DM 3068 has the ability to detect below 100 microvolts with the correct low impedance probes.

Seen in the Figure 4.4 below the current supply and the voltage was attached to the test specimen such that the current loop and voltage sensing loop are only linked through the binder jetted rod.

The rod was attached to the current supply by gator clips on the tips of the rod. The low impedance probes for the voltmeter were attached in-between these two gator clips. The distance 4.75 “ was measured using calipers for this distance between the two low impedance probes, and this distance is important later on for calculating the resistivity of the binder sintered copper.

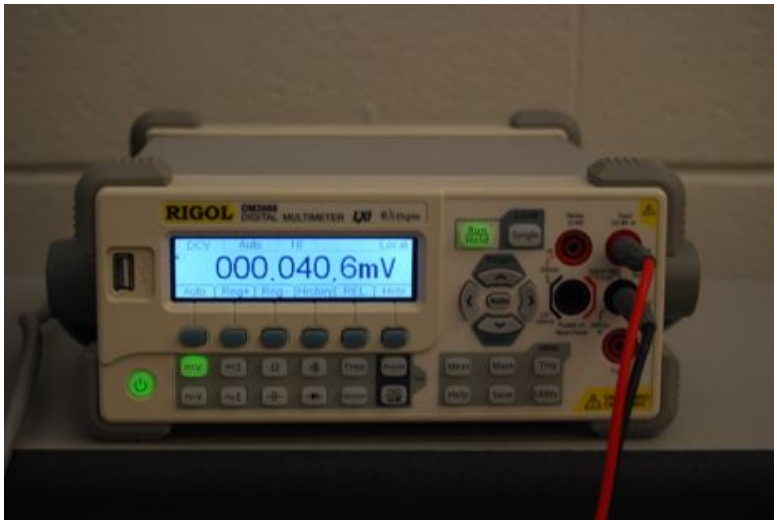

Figure 4.3: The Rigol DM3068 was used as a Voltmeter to calculate the Voltage drop over the test specimen.

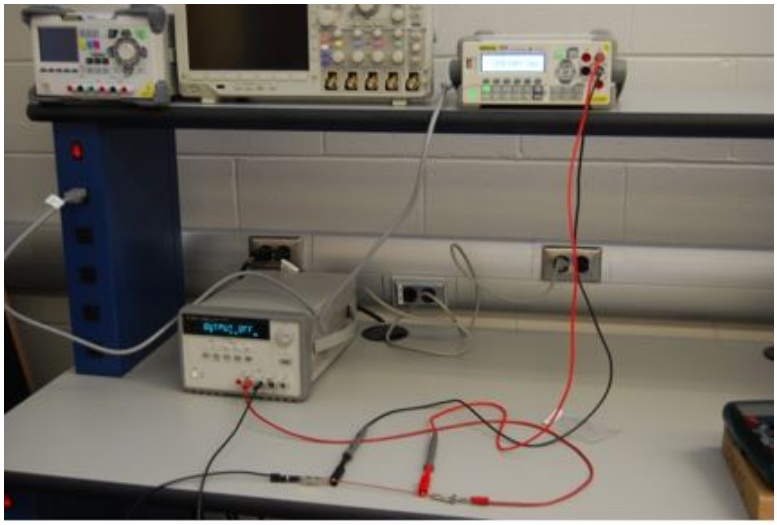

Figure 4.4: Seen in the figure is how the ammeter and voltmeter were connected to the test specimen.

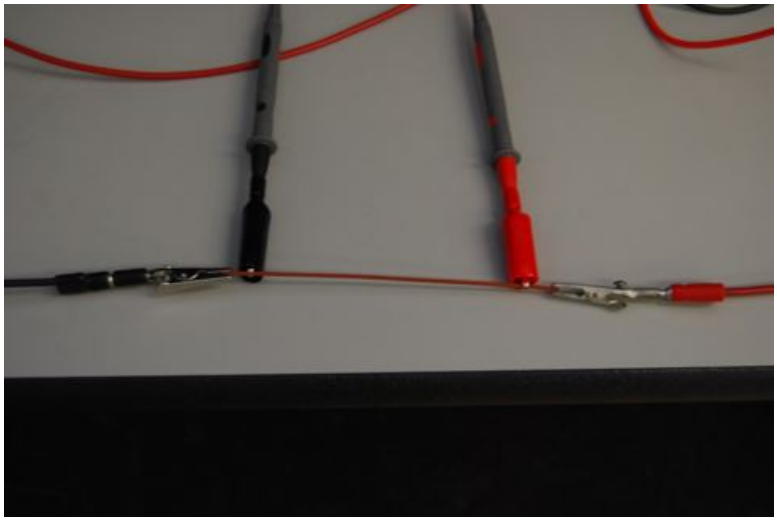

Figure 4.5: How the gator clips and low impedance probes were connected to the copper rod.

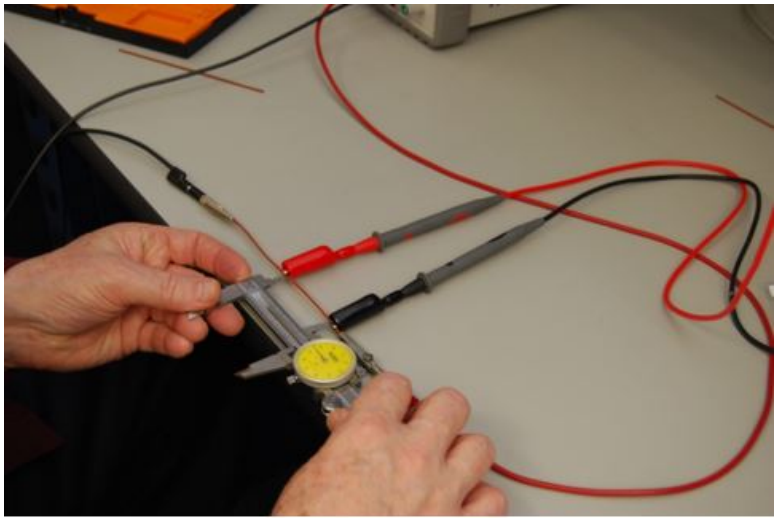

Figure 4.6: How the distance between the two voltage probes was obtained.

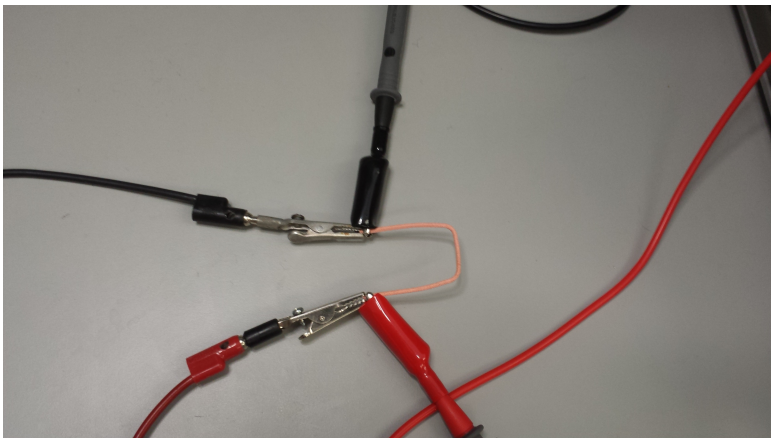

Figure 4.7: Measuring the electrical resistance of the batch 3 curved rods.

Chapter 5

Thermal Resistance Test Plan

To find the thermal resistance of the binder jetted sintered pucks, the Advanced Riko TC 1200 RH was used. For calibration of the machine a sapphire disk covered in the graphite spray is first placed into the test equipment. A series of three laser flashes are shot into the disk, first low, then medium, last full power of the laser. The average of all three of these tests are calculated to give the overall result of the test specimen. For the sapphire calibration disk, the values obtained are then matched to the given data of sapphire, and calibrated accordingly. Once calibrated the binder jetted copper pieces were placed into the laser flash rig and tested for their Cp and K values. Below are the steps used to prepare the copper pieces for testing.

To make sure the reflectivity of the binder jetted copper would not reflect any of the incoming laser flash, the test specimen were coated in the dry graphite film spray. The effect was the puck would not be the orange copper color, and would rather be a "flat black". This color will absorb a larger amount of energy than without the covering.

Seen in Figure 5.4 is a photo of placing the binder jetted copper pieces into the testing rig. Due to size constraints of this test apparatus the binder jetted copper pieces had to be printed 1cm in diameter and 1mm thick. Because of the tight tolerances of the laser flash diffusivity machine test jig seen in Figure 5.4 and Figure 5.5, it was important to know the percent shrinkage associated with the different sintering profiles discussed before.

After placing the test apparatus as shown atop the carrier tube, the whole assembly is slid up into the heater shown in Figure 5.6. It was important to make sure there was a good seal

Figure 5.1: The laser flash diffusivity machine

Figure 5.2: This is a photo of the graphite spray used on the sapphire and copper test pieces.

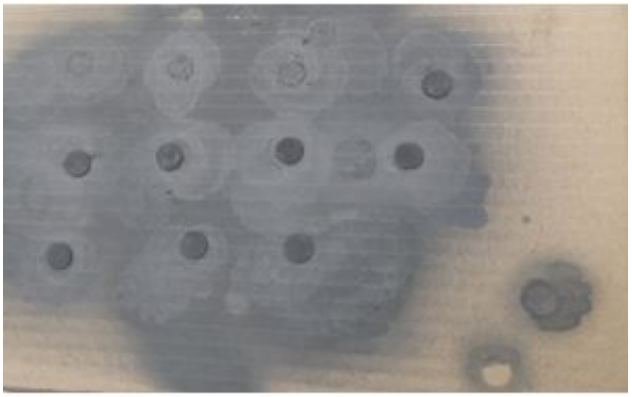

Figure 5.3: The even coating of graphite spray on both sides of the copper specimen.

Figure 5.4: Placing the binder jetted copper pieces into the testing rig.

when the carrier assembly was locked in because the test chamber in the heater is brought to a vacuum. If there was a poor seal on the gasket, the air within the test cell will add convection to the disk as it is being laser flashed, overall fouling the measurements of that specific test.

Figure 5.5: This is a photo of the test apparatus on top of carrier tube.

The heater, seen in Figure 5.6 was not used for the tests because the data was needed to be taken at 24 Celsius or room temperature. Reason for the heater is to be able to test different samples at temperature up into the thousands of degrees C. Future tests may possibly be undertaken which will use this heater to regulate these higher temperature tests.

After the test specimens are placed into the laser flash diffusivity machine, a series of three separate 1 Joule laser flashes are shot at the test disks. The first shot is a lower power test shot which is just below 1 Joule. The second is a medium power shot at 1 Joule. The last is a higher power shot at just above 1 Joule. These three test are then averaged into the final resultant test line as seen in before in the theory section.

Through these averaged lines, the laser flash diffusivity machine will use the mass and inputted disk width to then calculate the Cp, alpha, and K, using Equation 2.5 Equation 2.6 and Equation 2.7. The results of the laser flash diffusivity tests can be seen in the thermodynamic results section of this thesis.

Figure 5.6: This is the photo of the heater for the laser flash rig.

Chapter 6

Results

6.1 Electrical

Once the clips and probes were attached to the test specimen, the equipment was turned on, and voltage measurements were taken. For the measurements to be valid for the Wiedermann Franz Law the temperature of the metal has to be the same as the temperature during the thermodynamic measurements which is room temperature, or 24 degrees Celsius.

Due to the internal resistance within the metal and due to one of the gator clips having a high resistance, the copper sample would increase temperature of 4 C per minute. So calculations of the voltage where taken at room temperature and also at 30 C for the first batch, and only at room temperature for the second and third batch.

As a test to determine if there were any flaws in the print of the copper rod, sample 3 was chosen and at 30C the voltage was measured over the whole rod, on one end, and on the opposite end. This quick measurement ensures the uniformity within the copper rod print. As seen below in Table 6.1, the voltage different was split in the middle with an overall voltage resistance of 15.2 mV and with both sides 7.59 and 7.6 mV respectively.

Table 6.1: Resistivity uniformity throughout the rod in Batch 1

Sample	distance between leads (in)	Voltage Difference (mV)	Temperature (C)
3	4.75	15.2	30
3	2.375	7.59	30
3	2.375	7.6	30

Table 6.2: Data table for electrical results

Batch 1	mV	amps	L (m)	L (density)		Ave cm^2		Weight
1	14.344	10	0.0121	0.15494		0.0286		2.9262
2	14.336	10	0.0121	0.15460		0.0285		2.8766
3	14.184	10	0.0121	0.15453		0.0273		2.8935
Batch 2					A1(cm^2)	A2(cm^2)	A3(cm^2)	Weight
1	14.03	10	0.0121	0.1535	0.02536	0.02458	0.02701	2.905
2	13.978	10	0.0121	0.1535	0.02581	0.02315	0.02656	2.885
3	13.98	10	0.0121	0.1532	0.02439	0.02512	0.02665	2.954
4	12.63	10	0.0121	0.1527	0.03283	0.02710	0.03019	3.223
5	14.01	10	0.0121	0.1535	0.02493	0.02593	0.02665	2.902
Batch 3			Length(mm)			Ave(mm^2)		Weight
1	7.997	10	98.24	N/A		2.665E-06		2.3211
2	7.533	10	98.3	N/A		2.775E-06		2.4393
3	3.917	10	49.93	N/A		2.9E-06		1.4682
4	2.525	10	30.61	N/A		2.975E-06		1.0609

Table 6.3: Electrical Rod Density measurements

Batch 1	Density (g/cm^3)	Full Density (g/cm^3)	Density%
1	6.5857	8.96	0.735019
2	6.5162	8.96	0.727256
3	6.8567	8.96	0.765267
Batch 2	Density (g/cm^3)	Full Density (g/cm^3)	Density%
1	7.37524	8.96	0.8231
2	7.46303	8.96	0.8329
3	7.58890	8.96	0.8469
4	7.02047	8.96	0.7835
5	7.31479	8.96	0.8163
Batch 3	Density (g/cm^3)	Full Density (g/cm^3)	Density%
1	8.2626	8.96	0.9222
2	8.2759	8.96	0.9236
3	8.2636	8.96	0.9223
4	7.7430	8.96	0.8642

Figure 6.1 shows us four sets of data. The first is the batch 1 data which can be seen in the mid 70% density, and about 3.25 ohm meters, and are light blue circles. The second is the Batch 2 data which can be seen represented in orange diamonds. The third batch of printed copper points is seen as green squares. The NASA data [8] is seen in Figure 6.1

Table 6.4: Final Resistance Data

Batch 1	ohms (10^-3)	L(m)	Ave(m^2)	Resistivity($ohm * m$)
1	1.434	0.12065	2.8677E-06	3.409E-08
2	1.434	0.12065	2.85527E-06	3.392E-08
3	1.418	0.12065	2.7308E-06	3.210E-08
Batch 2	ohms (10^-3)	L(m)	Ave(m^2)	Resistivity($ohm * m$)
1	1.403	0.12065	2.4586E-06	2.859E-08
2	1.398	0.12065	2.3157E-06	2.682E-08
3	1.398	0.12065	2.5126E-06	2.911E-08
4	1.263	0.12065	2.7108E-06	2.837E-08
5	1.401	0.12065	2.5937E-06	3.011E-08
Batch 3	ohms (10^-3)			Resistivity($ohm * m$)
1	.7997			2.2511E-08
2	.7553			2.1256E-08
3	.3917			2.2739E-08
4	.3512			2.4530E-08

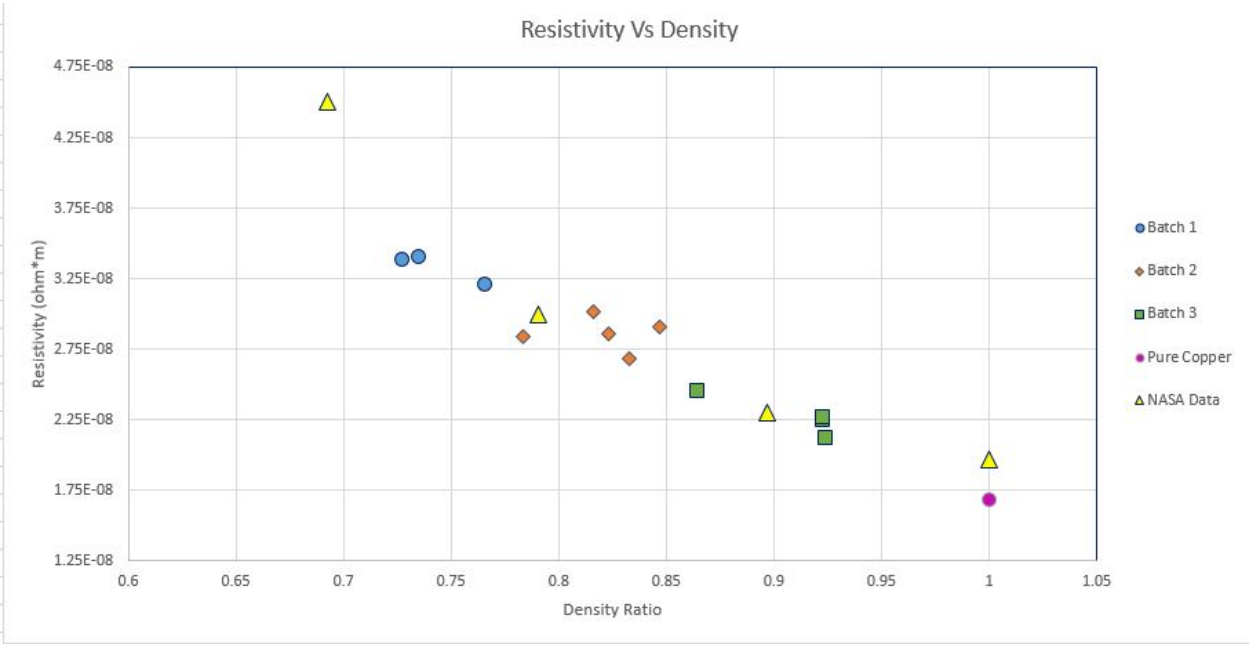

Figure 6.1: This is a figure showing the final result of the electrical resistivity tests

is represented as yellow triangles. The pure copper resistivity is represented by the purple point on the right above the density of 1.

As can be seen in the data from the 4 wire method shows a linear relationship between

the resistivity of copper and the density ratio. The NASA values however do not show this relationship, but do however verify that the values of our 4 wire test methods are within the correct range. The NASA testing procedures [8] for finding their resistivity's was not given, and therefore the reason for the discrepancy in results cannot be found. However for the purposes of finding the experimental values needed for the Wiedemann Franz Law, this thesis will use the linear data found from the experimental data.

6.2 Thermodynamic Results

Seen below in Figure 6.2 and Figure 6.3 are the two plots which would be received by the laser flash machine. The first figure shows an initial peak from the laser flashing the first side of the test sample. Seen afterward is a steep rise to the maximum temperature obtained by the laser flash rig and can be seen in the data represented by the red dashed line. Half of the time taken to reach the maximum temperature is seem as the 0.5 point in red on the figure, and this time is used in the equations to find the alpha needed in Equation 2.6

Notice the amount of noise in the temperature data after the second rise of the blue line. Because finding the temperature in this variation is difficult, a line of best fit is added to the data and the correlation of the line to the data is seen in the shape factor in the bottom right corner of the graph. The shape factor of this specific data sample is seen below in Figure 6.2 in the bottom right hand corner of the figure.

As can be seen above from the figure the half time for this sample is 1.73 ms with an R2 value of 0.9922.

Seen in Figure 6.3 above is the extended time vs temperature graph which is just a time extension from Figure 6.2. The two data points seen highlighted above are the two temperature and time data points used to find the delta t needed in Equation 2.4.

As can be seen in the figure above the half time for this sample is 2.0 ms with an R2 value of 0.9899.

Seen in Figure 6.5 above is the extended time vs temperature graph which is just a time extention from Figure 6.4. The two data points seen highlighted above are the two temperature and time data points used to find the delta t needed in Equation 2.4.

Seen in Figure 6.2 and Figure 6.4 there is a spike in the beginning of the laser flash diffusivity

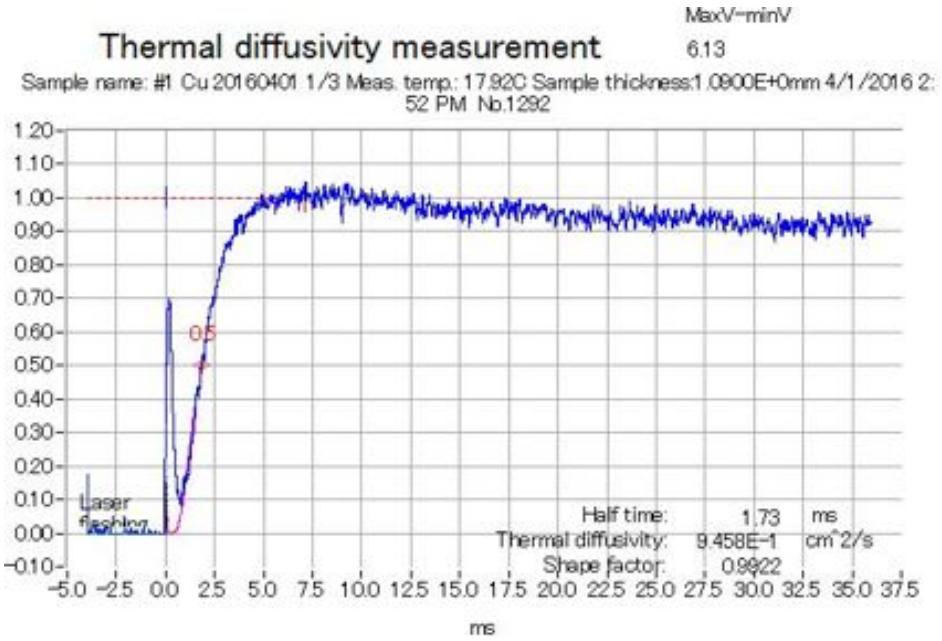

Figure 6.2: Laser flash diffusivity data from sample 1.

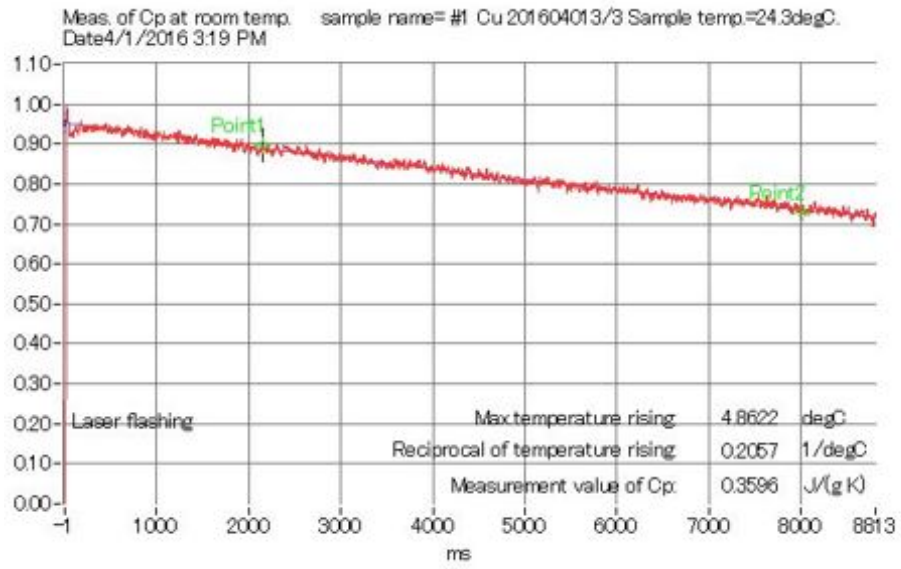

Figure 6.3: Time Vs. Temperature graph used to find Cp.

measurement. This spike is electromagnetic interference caught by the infrared detector from the pulse of the laser [32]. Some of the other laser flash diffusivity machines have an EMI corrector to remove the pulse.

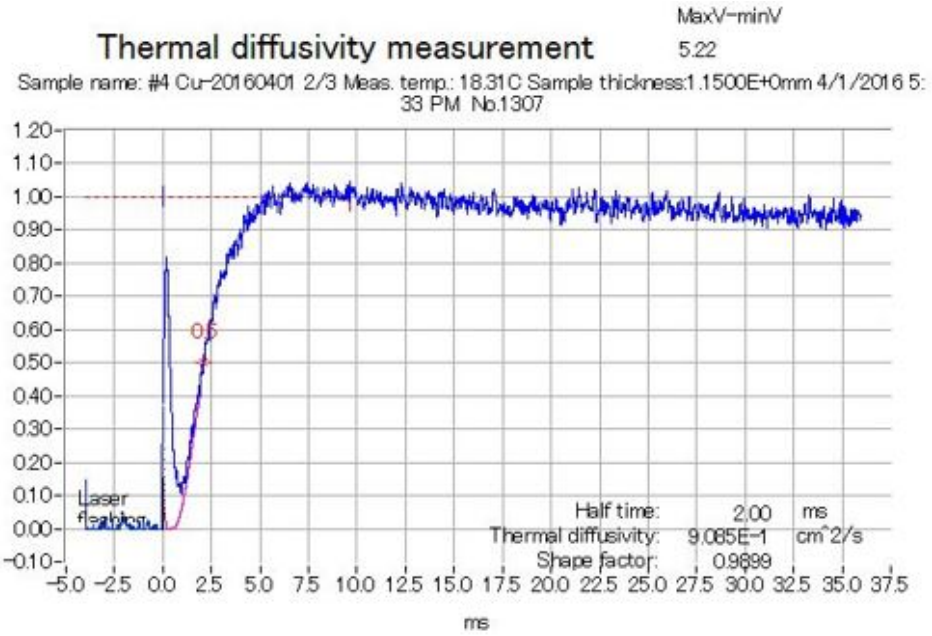

Figure 6.4: This is a graph of the data which came off of copper sample 1.

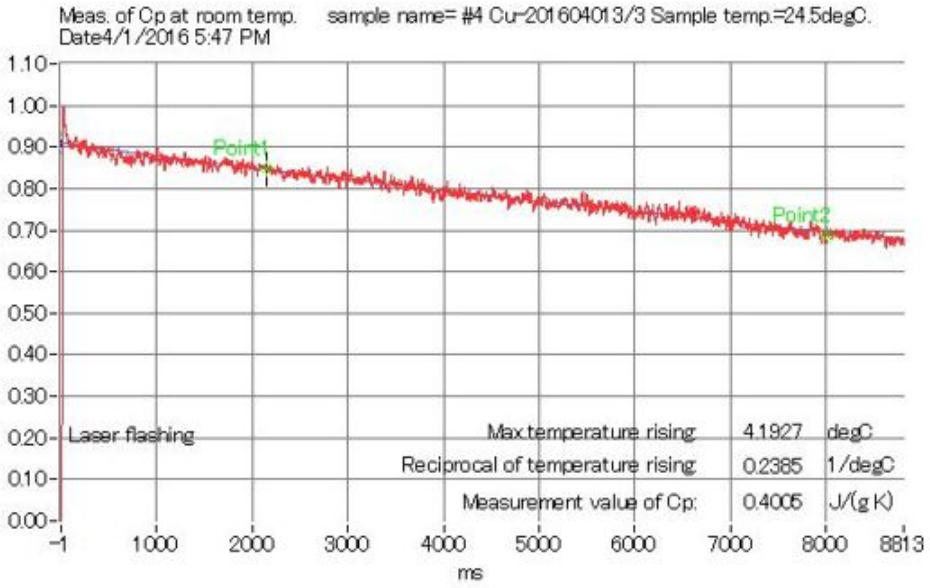

Figure 6.5: This is a graph of the data post laser flash, and from these two point the Cp value is obtained.

Table 6.5: Thermodynamic data Batch 1

Sample	Density %	Therm Cond. in WmK	Area mm$\hat{2}$
1	0.7583	226.024	84.05
2	0.7288	215.043	84.29
3	0.7384	220.350	84.45
4	0.7121	229.380	86.17
5	0.7076	201.402	89.08
6	0.6606	151.537	91.77
7	0.7514	199.641	84.70
8	0.6471	252.423	84.78
9	0.7481	219.952	84.78
10	0.6751	186.723	87.33
11	0.6765	156.739	91.86

Table 6.6: Thermodynamic data Batch 2

Sample	Density %	Therm Cond. in WmK	Area mm$\hat{2}$
1	0.7931	203.790	82.90
2	0.8005	192.930	82.59
3	0.8246	190.998	82.34
4	0.7952	211.422	83.07
5	0.7841	181.454	83.64
6	0.8044	187.959	83.15
7	0.8036	204.578	83.31
8	0.7984	193.768	83.72
9	0.8043	194.384	83.07
10	0.7869	209.137	83.96
11	0.8010	226.036	83.15

After all the calculations have been performed for both batches of sample disks there was a large variance in the data.

Some of the data points with the lower densities had the larger thermal conductivities. This was reversed from what the theory says what should happen, and therefore a variability study was performed on the data from both batches of disks. Interestingly enough it is found that the variability of the shrinkage of the disks in the sintering process was not as uniform as originally thought. If sintered correctly the 12 mm diameter disks should with a 20% shrinkage should have a top area of approximately 78.539 mm2. However all the sample disks had areas in the 82 to 92 mm2 range. This increase and large spread of areas accounted for the large range of thermal conductivity values.

Table 6.7: Thermodynamic data Batch 3

Sample	Density %	Therm Cond. in WmK	Area mm$\hat{2}$
1	0.9166	314.8547	88.08
2	0.933	376.9408	87.91
3	0.916	371.6678	87.75
4	0.9275	310.2776	88.91
5	0.9244	310.668	88.58
6	0.9097	379.901	86.59
7	0.9197	310.3474	89.58
8	0.9215	325.1343	86.92
9	0.9304	348.0873	87.42
10	0.9158	283.4232	86.59
11	0.9144	341.5006	86.43
12	0.9165	359.4499	86.59

It is theorized that the water jacket used to keep the silicon seal from melting during sintering caused a temperature gradient within the kiln itself. Prof of this temperature gradient can be seen in Figure 6.6 as there are two distinct peaks in the data. Data samples 6 and 11 were closet to the door in their respective rows with data samples 1 and 7 being the farthest from the door. This temperature gradient caused the sintering temperature to drop low enough to hinder full sintering of the disks closer to the door.

This theory was then verified when the second batch of disks were placed on the back edge of the kiln close to each other to decrease the effect of temperature gradients within the kiln. And the results seen in Figure 6.6 of increased uniformity proves that the water jacket caused the large variation within the first batch of data samples. But again the surface area of the tops of the disks we not close to the 78.539mm2 needed for the ideal case of being close to the dimensions of the calibration disk.

As can be seen in the figure above, there is a strong inverse correlation to the size of the sample disk and the Thermal Conductivity K of the data. If the data is shown as K verses area, then a correlation line can be determined. The correlation line if shows that if all of the batch 1 data was milled down 200 microns to have a 10mm diameter overall, then the data would have showed the value of K around 277 W/m*K.

Thankfully, the second batch of data was more uniform than batch 1, which helped increase the precision of the thermodynamic data, however they were not accurate. What is meant by accuracy is again the area of the created disks is not at the 78 mm2 needed area but

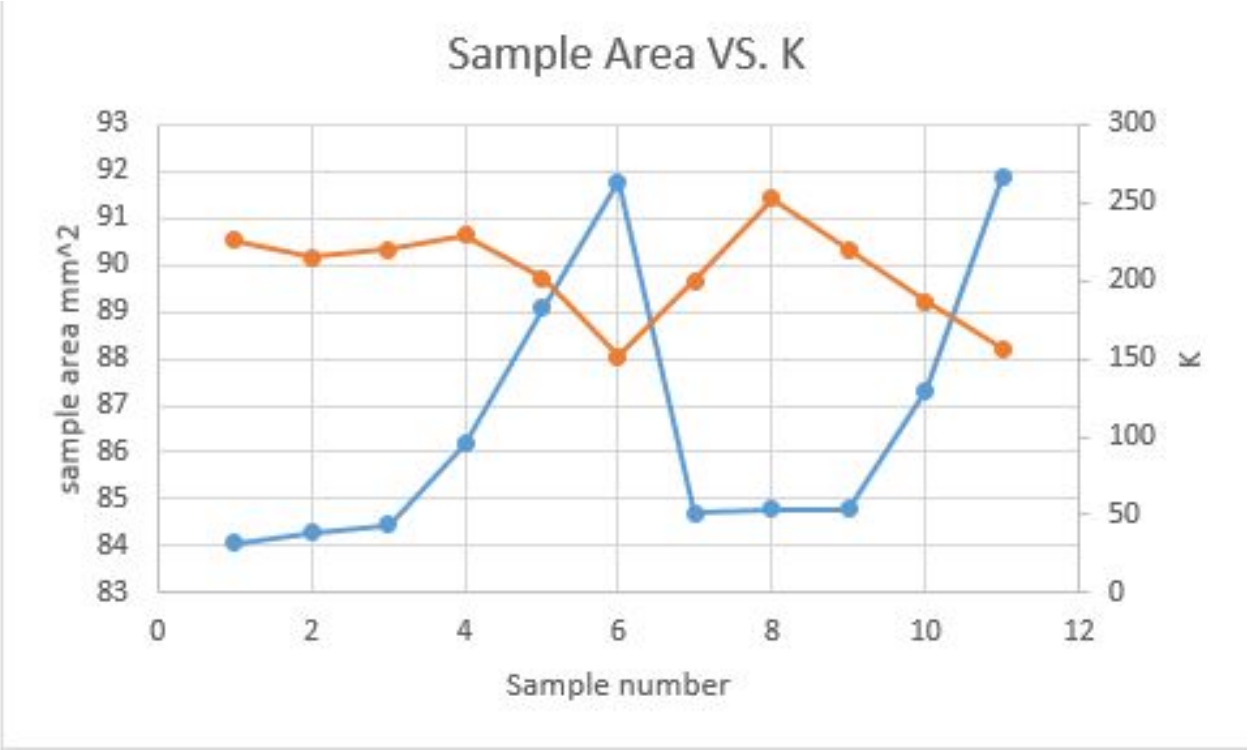

Figure 6.6: This is a figure showing the correlation of sample top area and Thermal Conductivity.

however close to 83 mm2. However in the scope of this thesis the raw data of all the tests will be used in the calculation of the new Wiedemann-Franz Law. Future research will need to be performed in order to verify the trend seen in Figure 6.6 and revise the thermodynamic data.

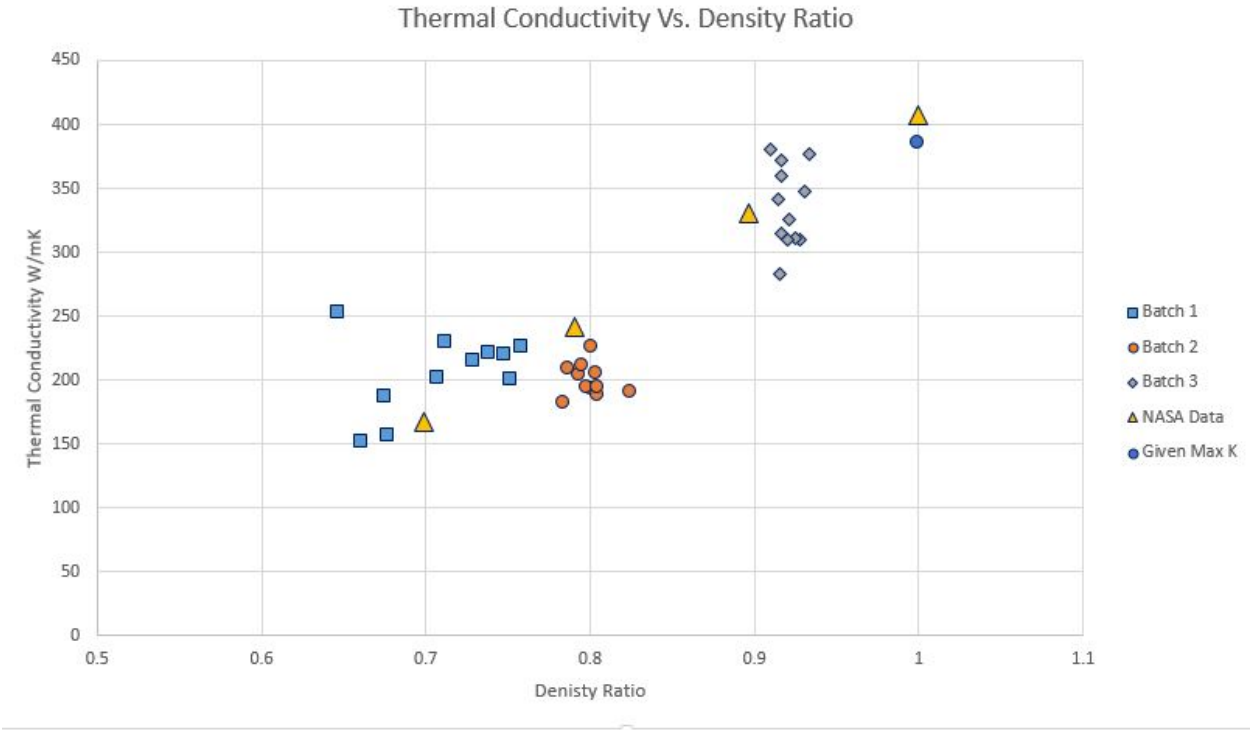

Figure 6.7: The results of the thermodynamic data

Chapter 7

Final Results

7.1 Equations

The conclusions of this data is that from the density of 70's percent range through to the 90's percent range the binder jetted copper performs with an increase of electrical conductivity, and an increase in thermal conductivity. The electrical resistivity decreased per density increase with the linear equation seen in Figure 7.1 and written out in Equation 7.1.

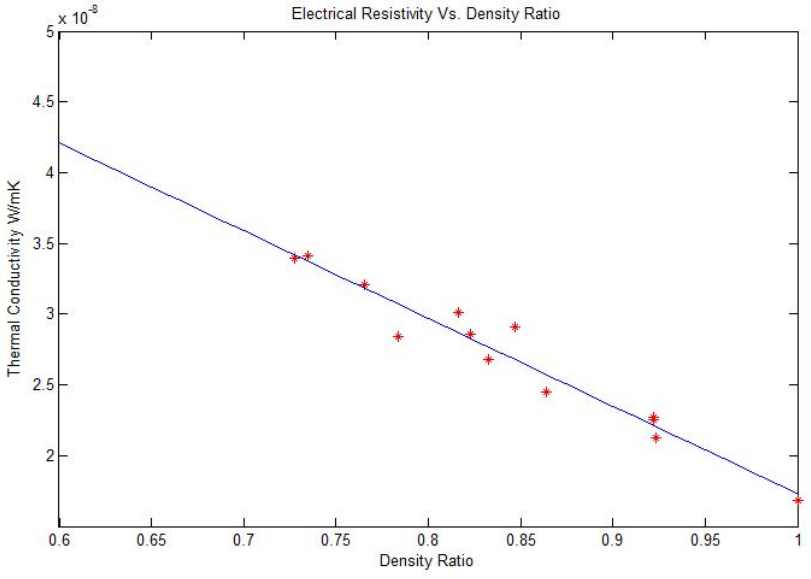

Figure 7.1: The linear line of best fit for the Electrical Resistivity Data

$$C = \frac{1}{-0.62E-07} * x + \frac{1}{0.7929E-07} \tag{7.1}$$

- C = Electrical Conduction.
- x = Density percentage (0 to 1).

The thermal conductivity of the specimens increased per density ratio increase with the overall trend between the data being hard to differentiate. However the trend seems to follow the NASA data [8] which is a linear increase per increase of density ratio. After the raw data from the thermodynamic runs was given a linear regression the line of best fit also fit the NASA data, therefore verifying the assumption made of a linear regression. The Figure 7.2 and the Equation 7.2 for the thermodynamic conduction verses density ratio can be seen below:

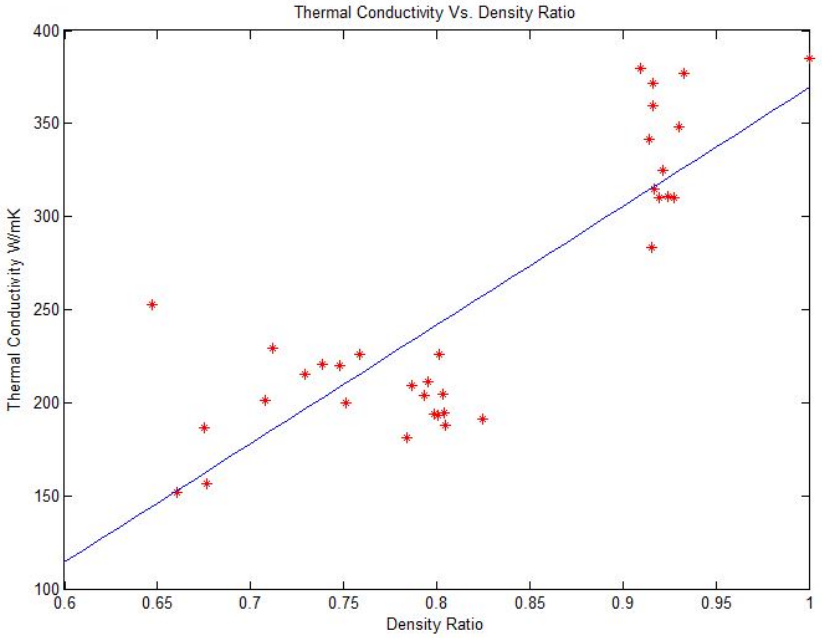

Figure 7.2: The linear line of best fit for the Thermal Conductivity Data

$$K = 638.0791x - 268.7404 \tag{7.2}$$

- K = Thermodynamic Conduction Coefficient.

- x = Density percentage (0 to 1) .

However the data from the thermal conductivity tests are not as linear as seen in the electrical data. The 70's percent density ratio data follows close to the linear regression line but however has an outlier

In the beginning of this thesis, the question of "Is there a relationship between density of BJC and the Overall Lorenz number of copper?" and "Can a mathematical relationship be created to model the thermal and electrical properties of BJC?" can be answered from the data shown. The Equation 7.1 and Equation 7.2 prove that there is a relationship between BJC and the density of the prints. Therefore the answer to the first and second questions is yes!

The linear relationship seen in the electrical resistivity measurements shows that an increase in density linearly decreases the resistivity of the metal. Within the thermodynamic tests the same trend is seen. With the linear increase in density, the resultant line is a first order polynomial. The model for this relationship could be increased up to a multi order polynomial, however the increase in degrees of freedom only increase the r2 value by a small amount. Therefore the first order polynomial was chosen due to the linear relation seen from the NASA data [8]. Overall the main point which needs to be taken away is that there is a relationship between density and the thermodynamic and electrical properties. And both of these relationships are linear, first order polynomials. Because a mathematical model can be found for the thermodynamic and electrical properties, the Lorenz number can be found as a function of density at 297.15 K.

$$M = \frac{638.0791x - 268.7404}{(\frac{1}{-.062E-07} * x + \frac{1}{0.7929E-07}) * 297.15} \tag{7.3}$$

- M = Modified Wiedemann-Franz Law to find modified Lorenz number
- x = Density ratio (0 to 1) .

Seen in Equation 7.3 is the Modified Wiedemann-Franz Law. This new law lets researchers input the calculated density ratio of their Binder Printed Copper part and have a modified Lorenz number to then calculate either the electrical or thermal conductivities using the prior Wiedemann Franz Law.

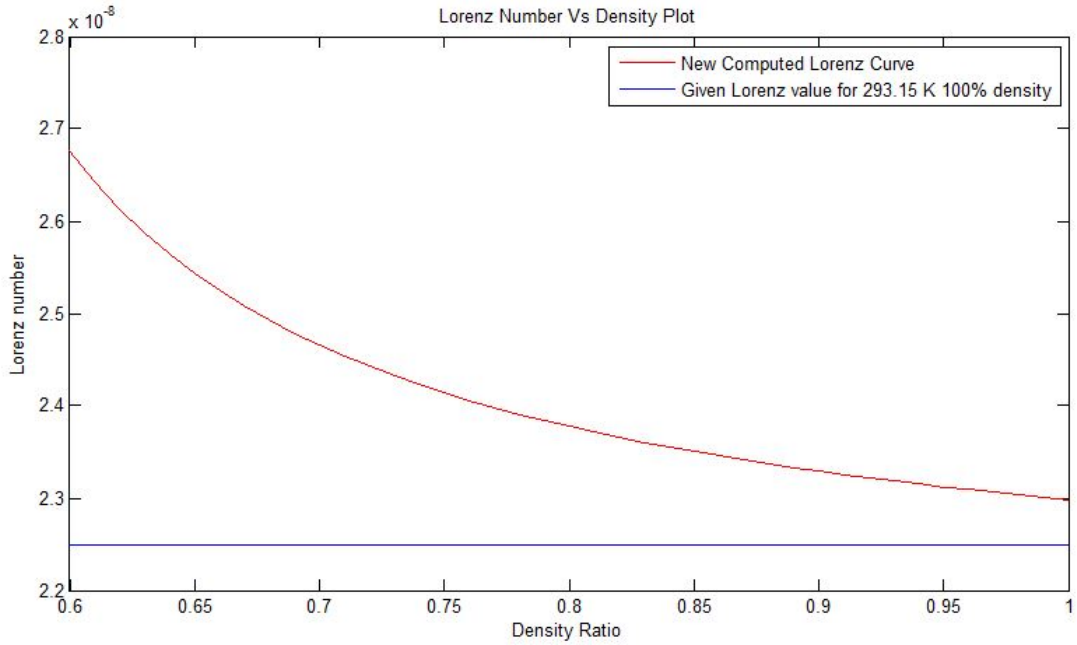

Figure 7.3: Equation 7.3 showing modified Lorenz number per density value vs. old Lorenz number for that temperature of copper

Seen in Figure 7.3 is the resultant line of the Modified Wiedemann-Franz law equation plotted next to the known Lorenz value for pure copper at 279.15 K. As can be seen the modified curve is not constant, and therefore this proves that for a more correct use of the Wiedemann-Franz Law researchers should use the Modified Lorenz number from this resultant thesis equation and not the given value of 2.25e–8 $W\Omega/K^2$. When the Modified Wiedemann-Franz law equation is used, the assumption of room temperature has to be used.

7.2 Discussion

The data from the thermal conductivity tests are not as linear as seen in the electrical data. The 70's percent density ratio data follows close to the linear regression line but however has an outlier down by the 64% density ratio mark. The cause for the large outlier in unknown, accept for the fact that the actual size and dimensions of the sample disks varied wildly within this data set. Discussed previously was the variation within the sample surface area, however this should not increase the thermal conductivity of the sample disks. It should actually perform the opposite reaction and decrease the resultant thermal conductivity value

of the sample. So the outlier seen at the 64% mark has to be deemed an outlier which at this time cannot be explained.

The 80's percent density ratio data performed oppositely as it should have, and actually decreased in thermal conductivity compared to the 70's percent density ratio data. However this data has much better precision, and better uniformity within sample sizes and weights. If an analysis is performed to augment the thermal conductivity data due to edge effects, the values should fall closer of not on the linear regression line seen in Figure 7.2. This however is a bias I have had ever since seeing the data fall below the linear regression line and needs to be tested.

Last the 90's percent data has a small variation within the density ratios but however has a large spread of values ranging from 285 – 385 W/mK. The small variation within the density ratios can be attested to placing the disks in the back of the kiln where there were less thermal gradients from the front doors cooling jacket. But the large variance within the data can be attested to the error in measuring all variables including the thickness of the sample d^2, and density of the disks.

The large thermal variability within the higher percentage of disks is not surprising however. Within academia there has been a large discrepancy between the thermal conductivity of copper. Some say the value is 385 W/mK [33] , and others that it is as high as 415 W/mK [34]. But the fact remains that measuring a metal with this high of a thermal conductivity is extremely difficult.

Also, in order for the new Wiedemann-Franz law to work, a few assumptions had to be made. The first assumption is that every disk and rod had their respective conductivities measured at precisely 297.15 K. The temperature of the two halls in which the data was taken were close to these values but had to be assumed exact. Second, that the vacuum within the laser flash diffusivity rig was a perfect vacuum. This would be quite difficult to achieve, but in order to remove convection cooling effects of the disks during testing, this perfect vacuum has to be assumed. Also, uniformity of the graphite spray across the disks. Unless weighed before and after, and measured before and after spraying, final thickness of the graphite on the disks will vary per disk. Fourth, the disks have to be flat. The 90's percent disks had curled within the kiln and therefore did not sit as perfect as they should have, therefore changing slightly the flux of the laser hitting the disks. Also the curling effects of the disks could have caused a pooling of the graphite after spraying. Needless to

say, the large assumption of perfectly graphite covered uniform flat disks had to be used.

Last, the assumption that both the electrical resistivity, and thermal conductivity are linear regressions at all. The only prior data to say if there is a correlation between the density ratio and thermal or electrical characteristics is the NASA paper from 1971 [8]. And this paper has the electrical resistivity data having more of a second order polynomial decrease, and a linear increase in thermal conductivity. My bias is therefore to accept the linear regression for the thermal conductivity data because of the larger r^2 value and less clear view of how the trend should be, and decline the second order polynomial regression for the electrical resistivity data due to the larger r^2 value towards the linear trend. Overall making both regressions for this thesis become linear.

However if all the assumptions from above are used, the resultant curve seen in Figure 7.3 comes close to the given Lorenz number at 297.15 K. Proving that Equation 7.3 is valid, and that also that the Wiedemann-Franz Law can be used within binder jet printed copper. Second this curve also means that the Modified Wiedemann-Franz law within this thesis is a more accurate way to use the law in the future.

Chapter 8

Future Work

There are many aspects of this research which need to be explored. Currently the only points which are used to find the equations above is 70%, 80%, 90% and 100%, and prior NASA data. Therefore there will need to be more density percentage points throughout the density range to increase the resolution of the overall equation.

With that being said, more points will be needed to increase the validity of the above equations, and more testing will be needed to increase the working range of the Modified Wiedemann-Franz law equation. Reason being, currently the equation given in this thesis is only for room temperature. With the use of this new material geared more towards electronics, or any other larger applications, the introduction of electricity will heat up the copper. Due to the resistance in the metal, the steady state temperature of the copper object will most likely never be at room temperature, and therefore tests will need to be conducted at much higher temperatures than room temperature.

Also there is a common procedure where binder jetted copper is infused with bronze to increase the density and strength of the final product. The lower melting temperature bronze will wick up into the porous copper within the sintering kiln if touching the BJC. Companies are currently using this technique to create high resolution sculpted metal door handles, and other complex bronze objects. Equations therefore for this infused bronzes thermodynamic and electrical properties most likely have not been calculated because the applications of this technology have not been in a thermodynamic or electrical use. Also besides just copper infused bronze, there are a couple other metals which can be binder jet printed. Studies as shown in this thesis therefore will need to be performed on metals such

as stainless steel, tungsten, and a couple others.

Besides just performing more tests on the different density copper, and also on different metals, a study on the performance of BJC at higher power ranges would be interesting to test. The temperature increase from the rods in this thesis was only from the higher resistance seen in the alligator clip and not the rod itself. It would be curious to see how the copper rod reacts to the higher power levels, and not just DC but AC as well.

Overall, BJC is an emerging technology which has not fully seen its capabilities yet. There are many different research areas as stated within this section which can, and should be researched so that binder jetting copper, and other such metals can fully be utilized in the future.

Bibliography

[1] Jeff McNair. *A historical background of AM*. URL: http://aaq.auburn.edu/node/1353.

[2] Terry Wohlers and Tim Gornet. "History of Additive Manufacturing". In: *Wohlers Report 2014 - 3D Printing and Additive Manufacturing State of the Industry* (2014), pp. 1–34. ISSN: 1098-6596. DOI: 10.1017/CBO9781107415324.004. arXiv: arXiv:1011.1669v3. URL: http://wohlersassociates.com/history2014.pdf.

[3] Maltesh Somasekharappa. *Additive Manufacturing - The Voxel Method*. URL: http://3dprintingindustry.com/news/additive-manufacturing-the-voxel-method-10349/.

[4] Ian Gibson, D.W. David W Rosen, and Brent Stucker. *Additive Manufacturing Technologies: Rapid Prototyping to Direct Digital Manufacturing*. Vol. 54. New York: Springer, 2009, p. 462. ISBN: 9781441911193. DOI: 10.1007/978-1-4419-1120-9. URL: http://www.amazon.com/Additive-Manufacturing-Technologies-Prototyping-Digital/dp/1441911197.

[5] Tracy McMahan. "NASA 3-D Prints First Full-Scale Copper Rocket Engine Part". In: *NASA Press Office* (2015).

[6] Yun Bai and Christopher B Williams. "An exploration of binder jetting of copper". In: *Rapid Prototyping Journal* 21.2 (2015), pp. 177–185. ISSN: 1355-2546. DOI: 10.1108/RPJ-12-2014-0180. URL: http://www.emeraldinsight.com/doi/abs/10.1108/RPJ-12-2014-0180.

[7] W.J. Sames et al. "The metallurgy and processing science of metal additive manufacturing". In: *International Materials Reveiws* (2016). URL: http://dx.doi.org/10.1080/09506608.2015.1116649.

[8] Thermal Conductivity and Resistivitv O F Porous. "THERMAL CONDUCTIVITY AND ELECTRICAL Resistivity of porous material". In: October 1971 (1971). URL: http://ntrs.nasa.gov/archive/nasa/casi.ntrs.nasa.gov/19720011984.pdf.

[9] Julian Rubin. *The Discovery of Ohm's Law*. 2013. URL: http://www.juliantrubin.com/bigten/ohmlawexperiments.html (visited on 06/23/2016).

[10] R Nave. *Resistance*. 1998. URL: http://hyperphysics.phy-astr.gsu.edu/hbase/electric/resis.html (visited on 07/11/2016).

[11] R Nave. *Superconductivity*. 1998. URL: http://hyperphysics.phy-astr.gsu.edu/hbase/solids/scond.html (visited on 06/23/2016).

[12] J. D. Fan and Yuriy M. Malozovsky. *Pauli Exclusion Principle*. 2013. DOI: 10.1142/S0217979213620245. URL: http://www.worldscientific.com/doi/abs/10.1142/S0217979213620245 (visited on 06/23/2016).

[13] Stanislav Dolgopolov. "Formation of Cooper Pairs as a Consequence of Exchange Interaction". In: *arXiv* 1.1 (2015), pp. 1–10. URL: https://arxiv.org/ftp/arxiv/papers/1501/1501.04978.pdf.

[14] Aristotle. *Aristotles's Rhetoric: Book II*. Ed. by Aristotle. first. Athens: Aristotle, p. 3. ISBN: 978-0823210497. URL: http://rhetoric.eserver.org/aristotle/rhet2-3.html.

[15] Miyamoto Musashi and Miyamoto Musashi. "The Book of the Five Rings: Go Rin No Sho". In: *The Book of the Five Rings: Go Rin No Sho* (1645).

[16] Paul Strathern. *Mendeleyev's Dream: The Quest for the Elements*. 2001, p. 308. ISBN: 0312262043. URL: https://books.google.co.uk/books/about/Mendeleyev%7B%5C_%7Ds%7B%5C_%7DDream.html?id=qCzoF9sjTkAC%7B%5C&%7Dpgis=1.

[17] Nicholas Clulee. *John Dee's Natural Philosophy: Between Science and Religion*. Routledge Kegan & Paul, 1989, p. 97. ISBN: 978-0-415-00625-5.

[18] Stephen. Wolfram. *A new kind of science*. Wolfram Media, 2002, p. 1197. ISBN: 1579550088.

[19] Robert Keim. *Kelvin (4-wire) Resistance Measurement*. 2014. URL: http://www.allaboutcircuits.com/textbook/direct-current/chpt-8/kelvin-resistance-measurement/ (visited on 07/11/2016).

[20] Fluke Corperation. "80 Series V Multimeters Users Manual Lifetime Limited Warranty". In: (2004).

[21] Rigol Technologies Inc. *Rigol Users Guide*. 1st ed. Beaverton, 2014, p. 167. URL: http://www.manualslib.com/manual/789392/Rigol-Dm3068.html%7B%5C#%7Dmanual.

[22] ASTM. *Standard Practice for Using a Guarded-Hot-Plate Apparatus or Thin-Heater Apparatus in the Single-Sided Mode 1*. Tech. rep. 2012, p. 9. DOI: 10.1520/C1044-12.

[23] Peter Krupa and Svetozar Malinaric. "Using the Transient Plane Source Method for Measuring THermal Parameters of Electroceramics". In: *International Journal of Mathematics, Computational, Physics, Electrical and Computer Engineering* 8.5 (2014). URL: http://waset.org/publications/9998149/using-the-transient-plane-source-method-for-measuring-thermal-parameters-of-electroceramics.

[24] C-Therm. *How it Works - C-Therm - Thermal Conductivity Instruments*. 2007. URL: http://www.ctherm.com/products/tci%7B%5C_%7Dthermal%7B%5C_%7Dconductivity/how%7B%5C_%7Dthe%7B%5C_%7Dtci%7B%5C_%7Dworks/ (visited on 07/12/2016).

[25] ASTM. *Standard Practice for Laser Flash Diffusivity Method*. Tech. rep. American Society for Testing and Materials, 2015, p. 10. DOI: 10.1520/E2585-09R15. URL: http://compass.astm.org/download/E2585.15523.pdf.

[26] Wolfgang Hohenauer. *Laser Flash Method to Determine Thermal Conductivity*. URL: http://www.phox.at/upload/Laser%20Flash%20Method%20to%20Determine%20Thermal%20Conductivity.pdf (visited on 07/12/2016).

[27] Robert Nave. *The Wiedemann-Franz Law*. 2000. URL: http://hyperphysics.phy-astr.gsu.edu/hbase/thermo/thercond.html (visited on 07/12/2016).

[28] John Daintith. *A Dictionary of Physics*. Ed. by Jonathan Law and Richard Rennie. Oxford University Press, Jan. 2015. ISBN: 9780198714743. DOI: 10.1093/acref/9780198714743.001.0001. URL: http://www.oxfordreference.com/view/10.1093/acref/9780198714743.001.0001/acref-9780198714743.

[29] Rob Nave. *Chemical Bonding*. 1999. URL: http://hyperphysics.phy-astr.gsu.edu/hbase/chemical/bond.html (visited on 07/12/2016).

[30] Michael Dayah. *Periodic Table*. 1997. URL: http://www.ptable.com/ (visited on 07/12/2016).

[31] Yun Bai, Grady Wagner, and Christopher B. Williams. "Effect of Bimodal Powder Mixture on Powder Packing Density and Sintered Density in Binder Jetting of Metals". In: *2015 Annual International Solid Freeform Fabrication Symposium* (2015), p. 62. ISSN: 1098-6596. DOI: 10.1017/CBO9781107415324.004. arXiv: arXiv:1011.1669v3.

[32] J-Q Liu et al. "Improvement on thermal diffusivity measurement repeatability of laser flash method". In: (2008). ISSN: 1000-1158.

[33] R Nave. *Thermal Conductivity*. 1999. URL: http://hyperphysics.phy-astr.gsu.edu/hbase/tables/thrcn.html (visited on 07/14/2016).

[34] W J Parker et al. "Flash Method of Determining Thermal Diffusivity, Heat Capacity, and Thermal Conductivity". In: *Journal of Applied Physics J. Appl. Phys. J. Appl. Phys. Phys. Lett* 32.19 (1961), pp. 1679–2596. DOI: 10.1063/1.1753717. URL: http://dx.doi.org/10.1063/1.1728417%20http://dx.doi.org/10.1063/1.1728417.